Ultrahigh surface density of Co-N_2C single-atom-sites for boosting photocatalytic CO_2 reduction to methanol

Minzhi Ma[a, b], Zeai Huang*[a, b], Dmitry E. Doronkin[c], Wenjun Fa[d], Zhiqiang Rao[b], Yanzhao Zou[b], Rui Wang[b], Yunqian Zhong[b], Yuehan Cao[b], Ruiyang Zhang[b], and Ying Zhou*[a, b]

[a] State Key Laboratory of Oil and Gas Reservoir Geology and Exploitation, Southwest Petroleum University Chengdu, 610500, China

E-mail: zeai.huang@swpu.edu.cn, yzhou@swpu.edu.cn

Fax: +86 28 83037406; Tel: +86 28 83037411

[b] School of New Energy and Materials, Southwest Petroleum University Chengdu, 610500, China

[c] Institute of Catalysis Research and Technology and Institute for Chemical Technology and Polymer Chemistry, Karlsruhe Institute of Technology Karlsruhe, 76131, Germany

[d] Key Laboratory of Micro-Nano Materials for Energy Storage and Conversion of Henan Province & College of Advanced Materials and Energy, Xuchang University Henan, 461000, China

* Corresponding authors: Zeai Huang (zeai.huang@swpu.edu.cn); Ying Zhou(yzhou@swpu.edu.cn)

Abstract:

Cobalt species as active sites for photocatalytic reduction of CO_2 to valuable products such as methanol have received increasing attention, however, it remains a huge challenge to achieve the high activity. Herein, a pyrolysis-induced-vaporization strategy was successfully employed to fabricate Co/g-C_3N_4 single-atom catalysts (Co/g-C_3N_4 SACs) with surface Co atom loading up to 24.6 wt%. Systematic investigation of Co/g-C_3N_4 SACs formation process disclosed that concentrated-H_2SO_4 exfoliation of g-C_3N_4 nanosheets (g-C_3N_4 NSs) as the substrate followed by a two-step calcination process is essential to achieve ultrahigh metal loading. It was found that the ultrahigh-density of Co single-atom sites were anchored on the g-C_3N_4 substrate surface and coordinated with two nitrogen and one carbon atoms (Co-N_2C). These single dispersed Co-N_2C sites on the g-C_3N_4 surface were found to act not only as electron gathering centers but also as the sites of CO_2 adsorption and activation, subsequently, boosting the photocatalytic methanol generation during light irradiation. As a result, the methanol formation rate at 4 h (941.9 μmol g^{-1}) over Co/g-C_3N_4-0.2 SAC with 24.6 wt% surface Co loading was13.4 and 2.2 times higher than those of g-C_3N_4 (17.7 μmol g^{-1}) and aggregated CoO_x/g-C_3N_4-0.2 (423.9 μmol g^{-1}), respectively. Simultaneously, H_2 (18.9 μmol g^{-1} h^{-1}), CO (2.9 μmol g^{-1} h^{-1}), CH_4 (3.4 μmol g^{-1} h^{-1}), C_2H_4 (1.1 μmol g^{-1} h^{-1}), C_3H_6 (1.4 μmol g^{-1} h^{-1}), and CH_3OCH_3 (3.3 μmol g^{-1} h^{-1}) products were detected over Co/g-C_3N_4-0.2 SAC. Besides, the photocatalytic activity of the Co/g-C_3N_4-0.2 SAC for the reduction of CO_2 to methanol was stable within 12-cycle experiments (~48 h). This work paves a strategy to boost the photoreduction CO_2 activity via loading ultrahigh surface density single atomically dispersed cobalt active sites.

Keywords: Cobalt, g-C_3N_4, single-atom catalysts, ultrahigh surface metal loading, photoreduction CO_2 to methanol

1. Introduction

Photocatalytic CO_2 reduction is identified as a two-birds-one-stone strategy to convert greenhouse gas CO_2 into value-added fuel chemicals, alleviating the pressure on the greenhouse effect as well as the dependence on fossil fuels [1]. Methanol (CH_3OH) is considered to be an ideal product for photocatalytic CO_2 reduction due to its convenient storage and transport with wide applications [2]. Photocatalytic CO_2 reduction to CH_3OH involves a 6-electron process, hence gathering a large number of electrons on photocatalyst surface is favorable to trigger high-performance CH_3OH formation [3]. Among the reported photocatalysts, using earth-abundant cobalt-based catalysts is beneficial to convert CO_2 [4]. Because cobalt is believed to capture CO_2 efficiently due to the strong hybridization between 2p orbitals of carbon/oxygen atoms and the 3d orbitals of cobalt atoms [5, 6]. Furthermore, cobalt atoms bonded with N/C atoms can act as active centers to gather electrons under light irradiation for enhancing CO_2 activation and reduction to CH_3OH [4, 7, 8]. However, bulk cobalt photocatalysts with limited surface-active sites of low atom-utilization efficiency are unfavorable to transfer and gather the photogenerated electrons at CO_2 photoreduction sites during light irradiation [9], leading to the limited efficiency of CO_2 reduction to CH_3OH.

Recently, single-atom catalysts with monodispersed Co-N_xC_{4-x} (x=0-4) coordination active motifs (Co-N_xC_{4-x}/substrate SACs) possess the merits of maximum atom-utilization efficiency, tunable electronic environments, high efficiency of charge transfer, and high electron mobility, which were reported to be beneficial for CO_2 reduction [10]. More importantly, the single dispersed Co-N_xC_{4-x} coordination moiety

usually results in an enrichment of photogenerated electrons on catalysts under light irradiation [2, 11, 12]. It can facilitate the multielectron process in the photoreduction of CO_2 to CH_3OH [13-15]. However, most reported Co-N_xC_{4-x}/substrate SACs of low Co loadings with a limited number of active sites are unfavorable to achieve high photocatalytic CO_2 reduction activity. Generally, increasing the cobalt loading is considered an effective solution strategy but cobalt atoms with high loadings are highly prone to migration and aggregation to CoO_x species with much low activity for photocatalytic CO_2 reduction [16]. Therefore, fabrication of highly-loaded Co-N_xC_{4-x}/substrate SACs (＞10 wt%) to achieve high photocatalytic activity is still extremely difficult [8, 17, 18].

Up to date, although several strategies to fabricate high metal loading of Co-N_xC_{4-x}/substrate SACs are achieved via direct pyrolysis of a nitrogenous organic compound and metal salt precursors [19, 20], most of the Co-N_xC_{4-x} single-atom sites exist in the bulk supports [8, 17, 21]. These single metal atoms in the support matrix can be only used as electron transport channels, but not as electrons gathering centers for photocatalytic CO_2 reaction on the surface [22, 23]. Subsequently, the CH_3OH production of photocatalytic CO_2 reduction showed a relatively low yield due to the limited surface-active sites. Therefore, designing and developing a strategy to fabricate ultrahigh surface loading cobalt single-atom catalyst with Co-N_xC_{4-x} coordination moiety is highly demanded but of great challenge for CO_2 photoreduction to CH_3OH.

Herein, we report a novel pyrolysis-induced-vaporization strategy for fabricating cobalt single-atom catalysts (Co SACs) with Co-N_2C coordination moiety and surface

cobalt loading as high as 24.6 wt%, which is a record value of all reported Co-N_xC_{4-x}/substrate SACs up to now. The as-synthesized Co/g-C_3N_4 SACs surface has extremely high monodispersed Co-N_2C active sites. As a result, it showed much higher activity for photocatalytic CO_2 reduction to CH_3OH in the absence of both sacrificial reagent and photosensitizer. This study provides new insights into the fabrication of high surface density of Co-N_xC_{4-x}/substrate SACs for highly photocatalytic CO_2 reduction activity to solar fuels.

2 Experiments

2.1 Materials

All used chemicals were analytical-grade reagents without any further purification before the experiment. $Co(NO_3)_2 \cdot 6H_2O$ and dicyandiamide were purchased from Aladdin Reagent Corp. Anhydrous H_2SO_4 (98%), absolute ethanol (95%), and silica sand (70-150 mesh) were purchased from Chengdu Kelong Chemical Reagent Corp. 99% ^{13}C enriched $^{13}CO_2$ was provided by Chengdu Keyuan Gas Corp. Dialysis bags were purchased from Viskase Corp (MD44, MW:3500).

2.2 Fabrication of g-C_3N_4 NSs catalyst

The bulk g-C_3N_4 was prepared using a thermal polymerization method [24]. Briefly, 20 g dicyandiamide was put into a porcelain calcination boat, then heated from 30 ^oC to 550 ^oC within 4 h and maintained at 550 ^oC for 4 h under an air atmosphere. After that, the products were cooled down to 50 ^oC naturally. The g-C_3N_4 NSs were synthesized *via* a modified method from the literature [25]. Firstly, 9 g bulk g-C_3N_4 was dispersed in 90 mL anhydrous H_2SO_4 and stirred for 1 h. Then, 90 mL of deionized

water was gradually added to the g-C_3N_4/H_2SO_4 mixture. Next, the clear solution was added to 300 mL absolute ethanol and stirred for 18 h. Finally, the sample was dialyzed to neutral with a dialysis bag (height: 30 cm, width: 6 cm, solution volume: 20 mL; membrane cutoff: 3500 kDa) in deionized water to remove both residual SO_4^{2-} and ethanol, then collected after drying at 60 ^oC.

2.3 Fabrication of Co/g-C_3N_4 SACs

The Co/g-C_3N_4 was prepared using $Co(NO_3)_2 \cdot 6H_2O$ and g-C_3N_4 NSs as the precursors. Specifically, the required amount of $Co(NO_3)_2 \cdot 6H_2O$ and 2.0 g of as-synthesized g-C_3N_4 NSs was mixed with deionized water. After drying on a hot plate, the obtained mixture was put into a semi-closed porcelain boat with a cover. The mixture was heated in a tube furnace to 130 ^oC within 11 min under Ar flow. It was kept at this temperature for 9 hours, then heated to 550 ^oC with a heating rate of 8.67 ^oC/min, and maintained at this temperature for 1 h. The sample was washed five times with 30 mL deionized water after cooling down. Cobalt atoms were successfully anchored on the surface of the g-C_3N_4 NSs during the pyrolysis-induced-vaporization strategy by a two-step calcination process. Fabricated samples were marked as Co/g-C_3N_4-x, where x was the desired weight ratio of Co atoms to g-C_3N_4 NSs. For example, Co/g-C_3N_4-0.2 refers to the desired weight ratio of Co atoms (0.4 g, the corresponding weight of $Co(NO_3)_2 \cdot 6H_2O$ precursor is 0.99 g) to g-C_3N_4 NSs (2.0 g) of 0.2.

For comparison, a sample was prepared using $Co(NO_3)_2 \cdot 6H_2O$ (0.99 g) and g-C_3N_4 NSs (2.0 g) at identical conditions but without an intermediate heating step (one-step calcination) at 130 ^oC for 9 h, was designated m-Co/g-C_3N_4-0.2. A sample prepared via

the one-step pyrolysis of the mixture of $Co(NO_3)_2 \cdot 6H_2O$ (0.99 g) and bulk g-C_3N_4 (2.0 g) was named T-Co/g-C_3N_4-0.2. Moreover, a sample fabricated using the $Co(NO_3)_2 \cdot 6H_2O$ (0.99 g) and the bulk g-C_3N_4 (2.0 g) at identical conditions was named CoO_x/g-C_3N_4-0.2.

2.4 Characterization

X-ray powder diffraction (XRD) patterns were obtained on a PANalytical X'pert diffractometer with Cu Kα radiation (40 kV, 40mA). The scanning electron microscopy (SEM) was performed on a JEOL JSM-7800F microscope. The transmission electron microscopy (TEM) and high-resolution TEM (HR-TEM) were collected on a Tecnai G2 F30 electron microscope operating at an accelerating voltage of 200 kV. The X-ray photoelectron spectroscopic (XPS) measurements were performed using a Thermo ESCALAB250Xi X-ray photoelectron spectrometer and all of the binding energies were calibrated to the C 1s level of adventitious carbon species (peak at lower binding energy) at 284.8 eV. Aberration-corrected high-angle annular dark-field scanning transmission electron microscopy (AC-HAADF-STEM) images and the related energy-dispersive X-ray spectra (EDX) were recorded on a Themis Z with an FEI Super X-EDX system and a double-corrected FEI Titan Themis TEM at 300 KV. The UV-vis diffuse reflectance spectra were recorded at room temperature on a Shimadzu UV-2600 spectrophotometer with an integrating sphere using Ba_2SO_4 as the reflectance standard. The photoluminescence (PL) spectra were measured using a fluorescence spectrophotometer (Hitachi F–7000FL). The Fourier-transform infrared (FT-IR)

spectra were acquired on a Nicolet 6700 spectrometer with samples pressed into KBr pellets. The CO_2 adsorption isotherms at 25 ^oC and CO_2 temperature-programmed desorption (CO_2-TPD) profiles of the samples (catalyst: 50 mg; carrier gas: Ar; temperature increasing rate: 10 ^oC min^{-1}; CO_2 adsorbed at 25 ^oC) were acquired on ASAP 2020 V4.00 and ASAP 2920, respectively. The samples were pretreated at 200 ^oC for 10 min at Ar atmosphere before CO_2 adsorption isotherms and CO_2-TPD tests. The products of the isotopic labeling experiment were analyzed by a quadrupole mass spectrometer (MS, Pfeiffer Vacuum OmniStar GSD 320 O1). Inductively coupled plasma optical emission spectroscopy (ICP-OES) measurements were performed on an Agilent 730 ICP-OES spectrometer to determine the concentration of metal species and elemental analysis (EA) was performed on a Vario EL III (Elementar) to determine the concentration of C, N, H, O, and S species. The simultaneous thermogravimetric-differential scanning calorimetry-mass spectrometer analysis (TG-DSC-MS) was used to study the formation process of Co/g-C_3N_4 SAC, conducted in a flow of Ar with a NETZSCH STA 449F3 thermal analyzer equipped with a QMS 403 D mass spectrometer. In addition, the mixture of $Co(NO_3)_2 \cdot 6H_2O$ (0.99 g) and g-C_3N_4 NSs (2.0 g) was kept at 130 ^oC for 1 hour during the TG-DSC-MS testing process.

X-ray absorption spectra (XAS) in terms of X-ray absorption near edge structure (XANES) and extended X-ray absorption fine structure (EXAFS) were measured at the CAT end station of the CAT-ACT beamline at the Synchrotron Radiation Source at KIT, Karlsruhe [26]. The samples were measured ex-situ at the Co K absorption edge in transmission mode in the form of pellets diluted with cellulose. The spectra were

normalized and the X-ray absorption fine structure spectra (EXAFS) background was subtracted using the ATHENA program from the IFFEFIT software package [27]. The k^3-weighted $\chi(k)$ data in the k-space ranging from 3-13 $Å^{-1}$ (multiplied by a Hanning window function with dk = 1.0 $Å^{-1}$) were Fourier transformed to obtain radial distribution functions (R space). To obtain the detailed structural parameters around Co atoms in the as-prepared samples, quantitative curve-fittings were carried out for the Fourier transformed $k^3\chi(k)$ in the R-space between 1.2 and 3 Å using the ARTEMIS module of IFEFFIT. Effective backscattering amplitudes F(k) and phase shifts $\Phi(k)$ of all fitting paths were calculated by the ab initio code FEFF 6.0. During the fitting of the Co/g-C_3N_4-0.2 sample, the amplitude reduction factor S_0^2 was fixed to the best-fit value of 1.00, and the Co-N coordination number (CN) was fixed to 2.0 and the Co-C coordination number (CN) was fixed to 1.0 while the interatomic distance (R), the Debye-Waller factor (σ^2), energy shift (δE_0), were allowed to vary. The fit quality was then evaluated using R-factor and reduced Chi-square. The wavelet transformed (WT) of EXAFS spectra were obtained using the WTEXAFS program [28].

2.5 Photocatalytic activity measurement

Photocatalytic activities of the as-prepared samples were evaluated in a closed system with a quartz window under ambient temperature and atmospheric pressure. The detailed information could be found in our previous report [29, 30]. In detail, 5.0 mg of the photocatalyst was firstly dispersed in 5 mL pure water in a Petri dish with an area of 44.2 cm^2, then dried at 90 ^oC. Then the sample was placed in the middle of the 276 mL reaction cell with a stirring bar at the bottom. Ar (99.999%) gas was flushed through

the reaction system to completely exchange the air and then both 4.0 mL of CO_2 (99.999%) and 1.0 mL H_2O were added into the reaction system. After that, the reactor was irradiated from the top using a 300 W Xe lamp (CEAULIGHT Co., Ltd., China) at the light intensity of ca. 1.5 W/cm^2. 1.0 mL of gas sample was taken out from the reactor every hour and used for the subsequent analysis by GC7900 gas chromatography (GC, Tian Mei Analytical Instrument Co., Ltd., China) equipped with a TXD-01 column, a nickel conversion furnace (NCF), a thermal conductivity detector (TCD) and a flame ionization detector (FID) to detect H_2, CO, and CH_4. $C_xH_yO_z$ products were determined by a 7890B gas chromatograph (GC, Agilent Technologies Inc., United States of America) with an HP/Plot-Q column. The photocatalytic CO_2 reduction activity experiments of each group were repeated at least three times. The isotope labeling experiments of $^{13}CO_2$ reduction with H_2O were performed under identical conditions with the reaction system described above.

2.6 In-situ diffuse reflectance infrared Fourier transform spectroscopy (DRIFTS) investigation

In-situ diffuse reflectance infrared Fourier transform spectroscopy (DRIFTS) measurements were performed at room temperature with a mixture of CO_2 (20% CO_2/Ar) and H_2O vapor (introduced by bubbling the gas flow through a water saturator at 40 °C). This study was carried out using a Bruker Tensor II instrument equipped with a Harrick High-Temperature cell [30-32]. The photocatalyst (30 mg) was pretreated at 200 °C for 15 min under 20 mL min^{-1} pure Ar gas (99.999%) flow. After that, CO_2 with H_2O vapor was continuously fed into the cell at 20 mL min^{-1} for 35 min. In the

circulation system, the mixture gas was allowed to reach adsorption-desorption equilibrium at the photocatalyst surface, and IR spectra were obtained every 1.5 min. After 35 min, the equilibrium was achieved, then the photocatalyst was illuminated with a PLS-FX300HU cold light lamp (Perfect light Co., Ltd., China; 700 mW cm^{-2}) under the moist CO_2 gas flow condition, and the data were collected at regular intervals of 1.5 min.

2.7 Photoelectrochemical measurements

All photoelectrochemical measurements were performed on a CH660E electrochemical workstation (Chenhua Instrument, Shanghai, China) equipped with a one-pot type cell with a three-electrode system. The saturated calomel electrode (SCE) was used as the reference electrode, and Pt wire was used as the counter electrode. The working electrode was prepared by a doctor blade method. The mixture of a photocatalyst and Nafion (5.0 wt%) was coated on a Fluorine-doped tin oxide (FTO) with a film thickness of ca. 50 μm and area of 4 cm^2, which was further treated at 90 ^oC for 3 h under Ar flow. Photocurrent-time and electrochemical impedance measurements of sample films at open circuit potential (OCP) were performed in 0.5 M Na_2SO_4.

2.8 Theoretical calculation method

Density functional theory (DFT) calculations were carried out using the CASTEP module in Materials Studio based on the plane-wave-pseudo-potential approach [33, 34]. The Perdew–Burke–Ernzerhof (PBE) functional of the generalized gradient approximation (GGA) was used as the exchange-correlation function [33, 34]. The

ultrasoft pseudo-potential was employed to describe the interaction between valence electrons and the core. A vacuum spacing of 15 Å was employed to eliminate interactions between layers. A kinetic energy cutoff of 380 eV and Monkhorst-Pack special k-point meshes of 3×3×1 were used to carry out geometry optimization and electronic structure calculation. The optimized lattice constant of the bulk g-C_3N_4 was a=b=4.74 Å and c=6.72 Å and the model structure containing from 1 to 7 cobalt atoms, 24 carbon atoms, and 32 nitrogen atoms. During the geometry optimization, all atoms were allowed to relax without any constraints until the convergence thresholds of maximum displacement (0.001 Å), maximum force (0.03 eV/Å), and energy (1.0×10^{-5} eV/atom) were reached [35]. The 2×2 supercell of monolayer g-C_3N_4 (001) was employed in the calculation.

3 Results and discussion

3.1 Structure and morphology of Co/g-C_3N_4

The as-prepared g-C_3N_4 without Co loading shows two representative diffraction peaks at around 12.6° and 27.9° corresponding to (100) and (002) planes, respectively (**Fig. 1a**) [24]. Introduction of Co to g-C_3N_4 caused a decrease in crystallinity, however, no peak shifts were observed in all samples, indicating that Co atoms were not doped into the g-C_3N_4 matrix (**Fig. 1a)** [36]. All diffraction peaks disappeared when the desired Co to g-C_3N_4 weight ratio was higher than 0.1, implying that the long-range order in the atomic arrangement of g-C_3N_4 was broken. The short-range order of g-C_3N_4 in Co/g-C_3N_4-0.2 was confirmed to be maintained via FT-IR and XPS analyses (**Fig. 1b-d**). The basic units of g-C_3N_4 such as CN heterocycle (1240-1649 cm^{-1}) and triazine

units (797 cm^{-1}) were observed in Co/g-C_3N_4-0.2 (**Fig. 1b**) [37-40]. The local framework composition of g-C_3N_4 such as the C-NH_x bonding structure, sp^2-bonded carbon in N=C-N, and bridging N atoms in N-$(C)_3$, and sp^2-hybridized nitrogen atoms in C=N–C still existed in Co/g-C_3N_4-0.2 (**Fig. 1c-d**) [41, 42]. In addition, the atomic ratio of C to N in the Co/g-C_3N_4-0.2 sample was detected to be around 0.66, which was close to the C/N ratio (0.62) in the g-C_3N_4 (**Table S1**). More importantly, obvious shifts to lower binding energy of C 1s, apart from the adventitious carbon species at 284.8 eV, and N 1s were observed in the Co/g-C_3N_4-0.2 sample (**Fig. 1c-d**) [43], implying that introduction of Co atoms to the g-C_3N_4 increased the electron density of C and N atoms, which is believed to be helpful to capture photogenerated electrons under light irradiation [11]. It is concluded that the structural skeleton of g-C_3N_4 was not destroyed and Co atoms strongly interact with g-C_3N_4 in the sample of Co/g-C_3N_4-0.2.

No peaks assigned to cobalt species were observed in XRD patterns of all samples prepared via the pyrolysis-induced-vaporization strategy after two-step calcination (**Fig. 1a**). However, the one-step calcination of cobalt nitrate with bulk g-C_3N_4 was easily aggregated to be CoO_x (T-Co/g-C_3N_4-0.2) (**Fig. 1a**), consistent with the previous literature [11]. The TEM images of g-C_3N_4 clearly show a thin-layer structure (**Fig. S1a**) without crystal lattice fringes (**Fig. S1b**). Thin layers were maintained in the Co/g-C_3N_4-0.2 (**Fig. S1c**). In addition, an obvious porous structure due to the H_2SO_4 exfoliation was formed in g-C_3N_4 and Co/g-C_3N_4-0.2. Similarly, the HR-TEM image of Co/g-C_3N_4-0.2 shows no crystalline lattices (**Fig. S1d** and inset of **Fig. S1d**). AC-HAADF-STEM image of the Co/g-C_3N_4-0.2 with bright folds and dark pores (**Fig. S2a**)

confirms the porous structure. The corresponding EDX mapping results demonstrated that carbon, nitrogen, and cobalt elements were homogeneously distributed, giving direct evidence of highly dispersed Co in the Co/g-C_3N_4-0.2 (**Fig. S2b-d**).

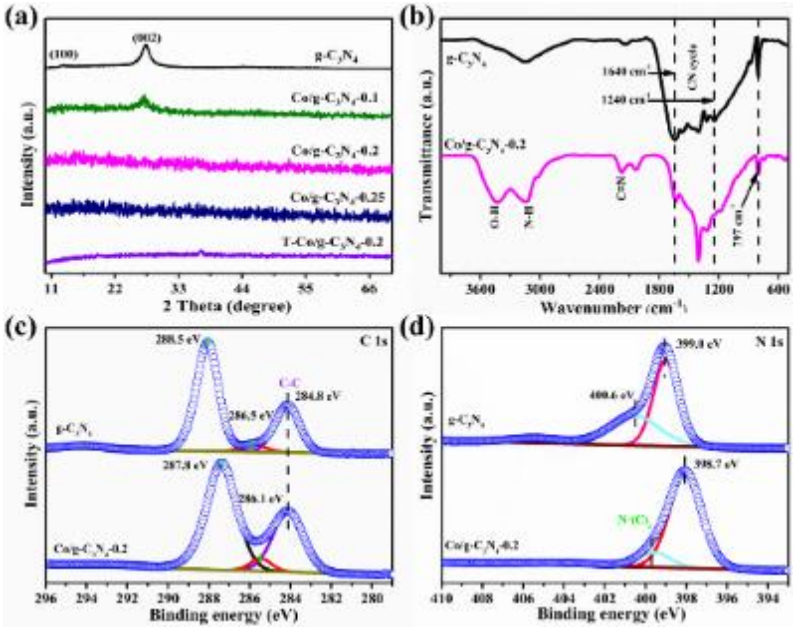

Fig. 1. (a) XRD patterns of as-prepared catalysts; (b) FT-IR spectra of g-C_3N_4 and Co/g-C_3N_4-0.2; high-resolution C 1s (c) and N 1s (d) XPS spectra of g-C_3N_4 and Co/g-C_3N_4-0.2.

AC-HAADF-STEM was conducted to further investigate the distribution of cobalt atoms in the Co/g-C_3N_4-0.2. The single bright dots can be ascribed to isolated metal atoms (**Fig. 2a and S3**). The AC-HAADF-STEM-EDX further proved that these dots are Co atoms (**Fig. 2b-e and S4**). XANES and EXAFS spectroscopy at Co K-edge were conducted to further study the local structure of Co atoms on Co/g-C_3N_4-0.2 (**Fig. 2f-g and 2i-j**). The Co K-edge region of the XANES spectrum of the Co/g-C_3N_4-0.2 was markedly different from the cobalt foil and Co_3O_4 reference spectra (**Fig. 2f**), however,

similar to that of the CoO and $Co(NO_3)_2 \cdot 6H_2O$ references, suggesting that the chemical state of Co in Co/g-C_3N_4-0.2 is +2. The high-resolution Co 2p XPS pattern (**Fig. S5**) of the Co $2p_{3/2}$ peak at 781.7 eV was ascribed to Co^{2+}, further proving that the oxidation state of Co on the g-C_3N_4 NSs surface was +2 [44-46]. Pre-edge XANES of Co peak at 7708-7709 eV in Co/g-C_3N_4-0.2 was slightly shifted to lower energy as compared to that of CoO and $Co(NO_3)_2 \cdot 6H_2O$ references (**Fig. 2f**). This might stem from the cobalt coordination to N and/or C atoms in Co/g-C_3N_4-0.2 other than the O atom because of the lower electronegativity of N and C elements as compared to the O element [12]. It is generally believed that O atoms bonded with metal could be gradually substituted by metal-N/C during g-C_3N_4 pyrolysis in an inert atmosphere [47]. Because the metal-O bonds possess less thermodynamically favorable under those conditions as compared to that of metal-N/C bonds [47]. Interestingly, Co_3O_4 was found to be transformed into CoN_xC_y *via* annealing of Co_3O_4 and g-C_3N_4 NSs mixture at 550 ^oC and Ar atmosphere (**Fig. S6**), proving that the Co-O bonds could be substituted by the Co-N and Co-C bonds during pyrolysis treatment. These results further suggested that cobalt atoms in Co/g-C_3N_4-0.2 tend to bond with carbon and nitrogen atoms rather than oxygen atoms.

The Fourier-transformed (FT) k^3-weighted EXAFS of Co/g-C_3N_4-0.2 displays a single peak at around 1.54 Å (uncorrected for phase shift), assigned to the coordination between cobalt and light elements such as nitrogen and/or carbon (**Fig. 2g**) [11]. It is worthwhile to mention that the FT EXAFS peak position of Co atoms in the Co/g-C_3N_4-0.2 was located at 1.54 Å, consistent with that of single atomically dispersed cobalt catalysts, such as Co(II) phthalocyanine (CoPc), other Co/g-C_3N_4 SACs, and Co-

N/carbon SACs [9, 11, 48, 49]. Nevertheless, it is significantly smaller than that of the Co^{II}-O position in $Co(NO_3)_2 \cdot 6H_2O$ (around 1.61 Å) and CoO (around 1.73 Å). More importantly, Co-Co scattering paths peak at around 2.17, and Co-(O)-Co scattering paths peak at around 2.61 were not observed in the Co/g-C_3N_4-0.2. These results strongly implied that cobalt species in the Co/g-C_3N_4-0.2 do not exist mainly in the form of Co phase /CoO_x clusters or nanoparticles. Eventually, in combination with the AC-HAADF-STEM and related mapping results (**Fig. 2a-e**), one can infer that the Co species were tentatively assigned to be single atomically dispersed on Co/g-C_3N_4-0.2 (Co/g-C_3N_4-0.2 SAC). This result was further validated by the wavelet transform (WT) analysis. The intensity maximum of Co foil and CoO is at around 6.7 $Å^{-1}$ assigned to Co neighbors, obviously different from Co/g-C_3N_4-0.2 SAC with only one intensity maximum at around 3.7 $Å^{-1}$ (light element such as O, C, N) was observed as shown in **Fig. 2h**. To give further insights into the coordination of Co in the sample of Co/g-C_3N_4-0.2 SAC, the corresponding FT EXAFS fitting was conducted to extract the structural information (**Fig. 2i-j**). The Co–N_2C coordination moiety with 2.07 Å of Co-N and 2.21 Å of Co-C average bond lengths gives a reasonably good fit of the experimental Co/g-C_3N_4-0.2 SAC EXAFS spectrum (**Table S2**). This is reasonable since Co-N_2 sites have been reported to be the most stable structure over Co-N-C SACs as found in both theoretical and experimental studies [12]. All the above results leading us to conclude that Co–N and Co-C bonds formed in the first coordination shell around Co on the Co/g-C_3N_4-0.2 SAC. In other words, single atomically dispersed Co sites with Co–N_2C coordination in the sample of Co/g-C_3N_4-0.2 SAC were successfully

fabricated.

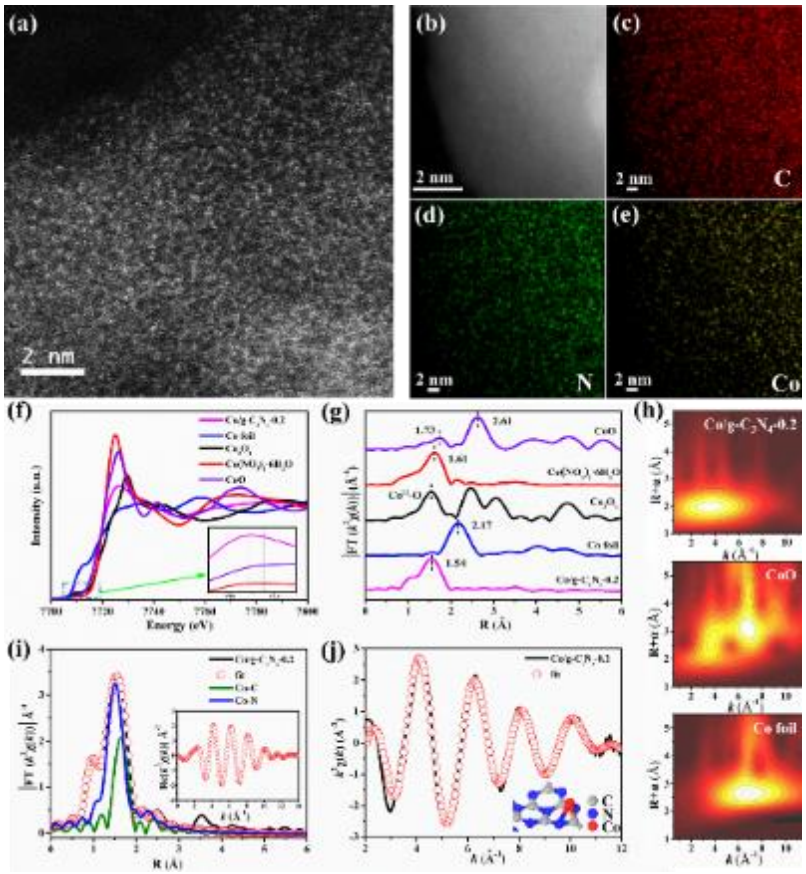

Fig. 2. (a) AC-HAADF-STEM image of Co/g-C_3N_4-0.2; STEM-EDX mappings of Co/g-C_3N_4-0.2 (scale bar: 2 nm) for (b) HAADF image, (c) C, (d) N, and (e) Co elements, respectively; **(**f) Co K-edge XANES spectra and (g) Fourier-transformed (FT) k^3-weighted EXAFS spectra (uncorrected for the phase shift) of Co foil, CoO, Co_3O_4, $Co(NO)_3 \cdot 6H_2O$, and Co/g-C_3N_4-0.2; (h) Wavelet transform (WT) of Co/g-C_3N_4-0.2, CoO, and Co foil; **(**i) Fit of the Co/g-C_3N_4-0.2 EXAFS spectrum in R-space and q-space (inset) with the contribution of individual shells (j) the same fit in k-space and the corresponding model structure (inset).

The loading amount of Co in the Co/g-C_3N_4-x samples was determined by ICP-AES (**Table S1**). The Co/g-C_3N_4-0.2 SAC showed an ultrahigh Co loading of 29.3 wt%,

which was a record value of the Co SACs (**Table S3**) [50]. Simultaneously, the corresponding surface Co loading is calculated by the XPS to be 24.6 wt% (6.9 at%). The maximum loading of single Co atoms in the heptazine-based 2×2 supercell of monolayer g-C_3N_4 (001) (32 N atoms and 24 C atoms) is calculated to be 6 atoms, in other words, the theoretical limit of the single Co atoms loading on the g-C_3N_4 is 32.5 wt%. This explains the fact that the second shell (Co-(O)-Co) as in CoO_x was observed by EXAFS in the Co/g-C_3N_4-0.25 sample with a Co concentration of 36.1 wt% (**Fig. S7**). The surface Co loading of Co/g-C_3N_4-0.2 SAC fabricated by pyrolysis-induced-vaporization strategy considerably exceeded that of previously reported Co/g-C_3N_4 SACs [50, 51]. Previously, it was reported that single atomically dispersed Co atoms on the g-C_3N_4 were more prone to aggregate to Co clusters during conventional Co SACs fabrication process with cobalt loading higher than 1.7 wt% [11]. Therefore, our strategy involving stepwise heating and g-C_3N_4 NSs as the substrate is an efficient method to fabricate Co/g-C_3N_4 SACs with ultrahigh surface loading of single atomically dispersed Co sites.

3.2 Mechanism of formation of Co/g-C_3N_4 SACs with ultrahigh surface loading

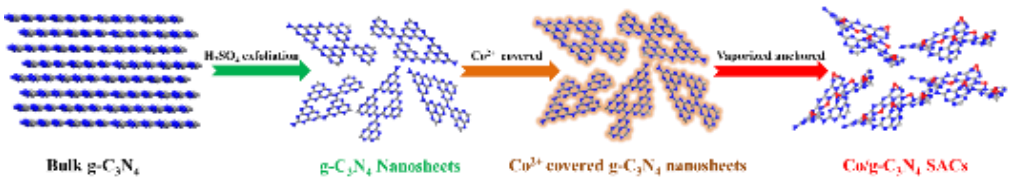

Scheme 1. The bulk cobalt nitrate vaporization induced by the pyrolysis process for the fabrication of Co/g-C_3N_4 SACs (blue: N atoms; grey: C atoms; red: Co atoms).

It is important to figure out the formation mechanism of the single atomically

dispersed Co sites with ultrahigh loading on g-C_3N_4. Two key points were found for achieving ultrahigh surface single cobalt atom loading of Co/g-C_3N_4 SACs: 1) porous g-C_3N_4 NSs as the substrate; 2) a two-step calcination process (**Scheme 1**). Firstly, the g-C_3N_4 NSs were prepared using concentrated H_2SO_4 exfoliation to obtain small porous structures (**Fig. S8**) [25]. The color of g-C_3N_4 NSs was completely converted from the faint yellow of bulk g-C_3N_4 to white (**Fig. S9**). The XRD peaks at around 12.6° and 27.9° corresponding to (100) and (002) planes were significantly decreased, suggesting that the g-C_3N_4 NSs have has smaller grains (**Fig. S10**) [52, 53]. Moreover, compared with bulk g-C_3N_4, the g-C_3N_4 NSs exhibits higher surface area and higher pore volume (**Table S1**). Simultaneously, CoO_x nanoparticles were found in the CoO_x/g-C_3N_4-0.2 sample fabricated using the bulk g-C_3N_4 as the substrate (**Fig. S11**). These results indicated that the g-C_3N_4 NSs surface could provide much more separated N_2C coordination sites for anchoring single atomically dispersed cobalt atoms and suppressing the cobalt atoms aggregation as compared to that of bulk g-C_3N_4.

Secondly, the aggregation of single atomically dispersed cobalt atoms during pyrolysis of the mixture of $Co(NO_3)_2 \cdot 6H_2O$ and g-C_3N_4 NSs process can be prevented by two-step calcination. The formation process of Co/g-C_3N_4 SACs during the two-step calcination procedure was studied using simultaneous TG-DSC-MS (**Fig. 3**). The g-C_3N_4 NSs showed only 4.0 wt% loss and no obvious endothermic peak in the range from 200 ^oC to 400 ^oC (**Fig. 3a**). However, the mixture of g-C_3N_4 NSs and $Co(NO_3)_2 \cdot 6H_2O$ precursors showed 30.9 wt% mass loss. A very broad endothermic peak at 300 ^oC was identified at this temperature range as exhibited in **Fig. 3b**, however

did not appear in the case of g-C_3N_4 NSs (**Fig. 3a**). This means that mass loss from 200 ^oC to 400 ^oC may be related to the decompose of $Co(NO_3)_2 \cdot 6H_2O$ (H_2O: *m/z*=17 and 18; N_2: *m/z*=28). Simultaneously, the single endothermic peak at 300 ^oC (**Fig. 3b**) is significantly different from the characteristic endothermic decomposition peak of the pure $Co(NO_3)_2 \cdot 6H_2O$ and the mixture of $Co(NO_3)_2 \cdot 6H_2O$ and bulk g-C_3N_4 (sharp peak at approx. 240 ^oC) as reported previously [54, 55]. Such a phenomenon might be ascribed to the vaporization and decomposition of $Co(NO_3)_x$ species. On the one hand, Co species with purple color was observed on the walls of the quartz tube after pyrolyzing (**Fig. S9d and S12a**). In contrast, almost none of the Co species were found in the quartz tube (**Fig. S12b**) when the sample of m-Co/g-C_3N_4-0.2 was fabricated by one-step calcination the mixture of g-C_3N_4 NSs and $Co(NO_3)_2 \cdot 6H_2O$ (**Fig. S9c**). Simultaneously, the CoO and/or $Co(OH)_2$ were generated on the sample of m-Co/g-C_3N_4-0.2 (**Fig. S13**). On the other hand, the mass percentage content of cobalt in the mixture of $Co(NO_3)_2 \cdot 6H_2O$ and g-C_3N_4 NSs precursors after calcination from 30 ^oC to 800 ^oC under Ar atmosphere followed by calcination at 800 ^oC for 1 h under Air atmosphere was found to be significantly decreased from 16.67 wt% to 10.34 wt% (**Fig. S14**). This indicates that a part of cobalt is taken away by Ar after vaporization. Moreover, the release of NH_3 (m/z=17) at around 530 ^oC during the calcination (**Fig. 3)** is potential evidence that the volatile Co species ($Co(NH_3)_x$) were formed by strong Lewis acid-base interaction between the single cobalt atom and NH_3 [56, 57]. Thus, one can infer that the two-step calcination method can efficiently inhibit the aggregation of single atomically dispersed cobalt atoms by inducing the vaporization of cobalt

species.

At the same time, the $Co(NO_3)_2 \cdot 6H_2O$ could completely infiltrate into small pores of g-C_3N_4 NSs (**Fig. S8a-d**) due to the low melting point of $Co(NO_3)_2 \cdot 6H_2O$ (55 ^oC) [54, 55] during the first calcination step at 130 ^oC (**Fig. S9c-d**). Therefore, the mixture of $Co(NO_3)_2 \cdot 6H_2O$ and g-C_3N_4 NSs precursors surface after the first calcination step at 130 ^oC was completely covered to $Co(NO_3)_x \cdot yH_2O$ crystals, clearly observed by the optical microscope (**Fig. S8a-b**). These results implied that the pyrolysis of the mixture of $Co(NO_3)_2 \cdot 6H_2O$ and g-C_3N_4 NSs precursors at 550 ^oC can further help to improve the single atomically dispersed cobalt atoms loading. This is mainly because the gas generated (such as NH_3, CO, NO, and $Co(NH_3)_x$, etc.) by the vaporization and decomposition of $Co(NO_3)_x \cdot yH_2O$ crystals process can expose more N_2C sites on the surface of g-C_3N_4. This point can be proved by BET. The surface area and pore volume of the as-prepared Co/g-C_3N_4-0.2 SAC (70.4 m^2/g, 0.37 cm^3/g) compared with the g-C_3N_4 (5.0 m^2/g, 0.016 cm^3/g) are enlarged by 14.1 and 23.1 times, respectively (**Table S4**). In addition, the surface area and pore volume of the as-fabricated Co/g-C_3N_4-0.1 SAC (18.6 m^2/g, 0.12 cm^3/g), Co/g-C_3N_4-0.25 (29.2 m^2/g, 0.21 cm^3/g) and CoO_x/g-C_3N_4-0.2 (27.7 m^2/g, 0.13 cm^3/g) also have some extent increased (**Table S4**).

Based on the above discussion, the formation mechanism of Co/g-C_3N_4 SACs with ultrahigh single atomically dispersed cobalt atoms was proposed as follows. Firstly, the porous g-C_3N_4 NSs provided sufficient sites for the adsorption and anchoring of cobalt atoms. Secondly, the pretreatment step at 130 ^oC for 9 h was vital to remove water from the mixture of $Co(NO_3)_2 \cdot 6H_2O$ and g-C_3N_4 NSs precursors, besides, Co atoms in

$Co(NO_3)_2 \cdot 6H_2O$ were coordinatively unsaturated to anchor on the g-C_3N_4 surface. Thirdly, the extra unanchored cobalt atoms were vaporized from the surface of g-C_3N_4 during the pyrolysis process. As a result, inhibiting the aggregation of cobalt atoms in the process of higher temperature annealing was achieved. Finally, the high amounts of single atomically dispersed Co atoms were uniformly distributed on the surface of Co/g-C_3N_4-0.2 SAC (**Scheme 1**). Therefore, the pyrolysis-induced-vaporization strategy and g-C_3N_4 NSs as the substrate were of great significance for the fabrication of Co/g-C_3N_4 SACs with high surface Co loading.

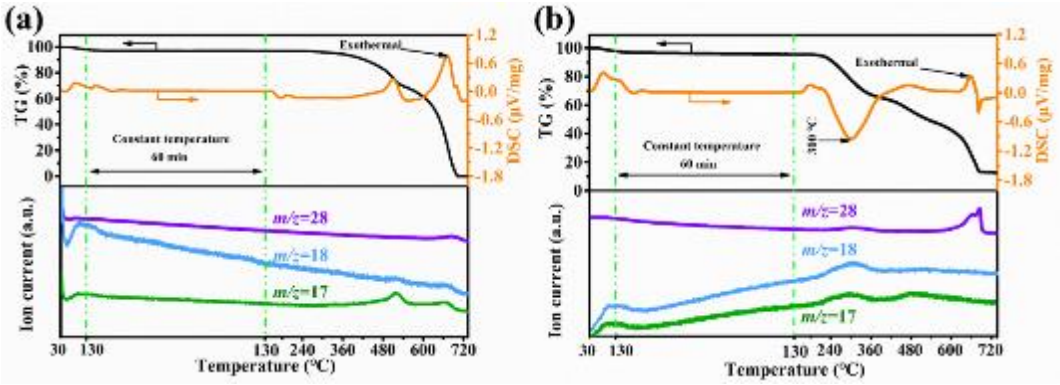

Fig. 3. Simultaneous TG-DSC-MS curves of (a) g-C_3N_4 NSs, (b) the mixture of g-C_3N_4 NSs, and $Co(NO_3)_2 \cdot 6H_2O$.

3.3 Photocatalytic CO_2 reduction

It is generally believed that cobalt species supported on g-C_3N_4 show high photocatalytic activity in CO_2 reduction [16], therefore the as-prepared catalysts were evaluated for the photocatalytic CO_2 reduction with H_2O in the absence of both sacrificial reagent and photosensitizer. The formation rates of H_2, CO, CH_4, C_2H_4, C_2H_6, C_3H_6, CH_3OCH_3, and CH_3OH products were evaluated (**Fig. 4**). However, it was

difficult to quantify the O_2 content due to the high oxygen detection limitation using the TDX-01 column. As shown in **Fig. 4a**, the Co/g-C_3N_4-0.2 SAC sample exhibited the highest CH_3OH (941.9 μmol g^{-1}) generation rate at 4 h and the CH_3OH selectivity was as high as 96.2%, which is 13.4, 2.6, 2.3, and 2.2 times higher than those of g-C_3N_4 (70.7 μmol g^{-1}), Co/g-C_3N_4-0.1 SAC (356.9 μmol g^{-1}), Co/g-C_3N_4-0.25 (415.4 μmol g^{-1}), and CoO_x/g-C_3N_4-0.2 (423.9 μmol g^{-1}), respectively (**Fig. 4**).

The low Co loading in Co/g-C_3N_4-0.1 SAC resulted in lower photocatalytic activity due to the low concentration of single dispersed Co-N_2C active sites (**Fig. 4, Fig. S7, Fig. S15a, and Table S1**). High loading of Co atoms, however, also led to poor activity, this may be due to reduction of active-atom-site numbers, followed by the reduction of the catalytic activity (**Fig. 4, Fig. S7, and Fig. S15b**) [16, 58]. Furthermore, the aggregation Co loaded on the bulk g-C_3N_4 (CoO_x/g-C_3N_4-0.2) also resulted in lower photocatalytic activity for photocatalytic CO_2 reduction (**Fig. 4, Fig. S7, and Fig. S15c**). Previous work demonstrated that CoO_x with lower active species showed lower activity for photocatalytic CO_2 reduction as compared with the single atomically dispersed Co sites [16, 58]. These results indicated that the high-density single dispersed Co-N_2C active sites are crucial for the photoreduction of CO_2 to methanol with high selectivity and activity. In addition, the ultrahigh density of single dispersed Co-N_2C active sites showed the stable formation of CH_3OH and suppress the CH_3OH peroxidation (**Fig. 4b**).

The high density single dispersed Co-N_2C active sites also facilitated the generation of H_2 (18.9 μmol g^{-1} h^{-1}), CO (2.9 μmol g^{-1} h^{-1}), CH_4 (3.4 μmol g^{-1} h^{-1}), C_2H_4 (1.1 μmol

$g^{-1}\,h^{-1}$), C_3H_6 (1.4 μmol $g^{-1}\,h^{-1}$), and CH_3OCH_3 (3.3 μmol $g^{-1}\,h^{-1}$) (**Fig. 4c**). Furthermore, when $^{13}CO_2$ was used as the feed gas, related ^{13}C products were formed (**Fig. S16**). Blank tests exhibit that CO_2 photoreduction products were no detected without either light or photocatalyst or reactant. These results confirmed that methanol was mainly generated from CO_2 reduction rather than an external pollutant carbon source. Impressively, as exhibited in **Fig. 4b**, our sample showed high stability of photocatalytic reduction of CO_2 to CH_3OH after 12 cycles (~48 h), the activity loss of methanol was almost negligible and there was no significant decrease in by-products except H_2, CH_4, and CH_3OCH_3 (**Fig. S17-S18).** From the XPS and XRD data, it was observed that the basic structure skeleton of Co/g-C_3N_4-0.2 SAC was not significantly changed after the 48 h reaction (**Fig. S19a-d**). As shown in **Fig. S19e**, the mass loss of Co/g-C_3N_4-0.2 SAC after reaction from 20 to 230 ℃ was only 0.2 wt%, which is mainly caused by desorption of water adsorbed on the surface. More importantly, it is worth noting that the Co/g-C_3N_4-0.2 SAC showed an obvious mass loss when higher than 450 ℃, indicating that the Co/g-C_3N_4-0.2 SAC showed a very high thermal stability in the process of the photocatalytic reaction process. This could be one of the reasons why the Co/g-C_3N_4-0.2 SAC maintained stable photocatalytic activity in the process of catalytic reduction of CO_2 to methanol.

The specific generation rates of different products for CO_2 reduction under similar reaction conditions over recently reported photocatalysts with single atomically dispersed cobalt sites (Co SACs) were compared (**Table S5**). For the Co/g-C_3N_4-0.2 SAC in our work, the CH_3OH generation rate and CH_3OH selectivity in the

photocatalytic CO_2 reduction was excellent among the reported Co SACs and some other similar photocatalysts [16, 59, 60]. Moreover, it is worth noting that the photocatalytic activity for the reduction of CO_2 to CH_3OH over Co/g-C_3N_4-0.2 SAC was close to that of RuSA-MC_3N_4 (**Table S5**) because Co/g-C_3N_4-0.2 SAC can provide the ultrahigh density of single dispersed Co-N_2C active sites [61]. Therefore, the Co/g-C_3N_4-0.2 SAC with an ultrahigh density of single dispersed Co-N_2C sites could achieve the high activity, high selectivity, high stability for photoreduction of CO_2 to methanol.

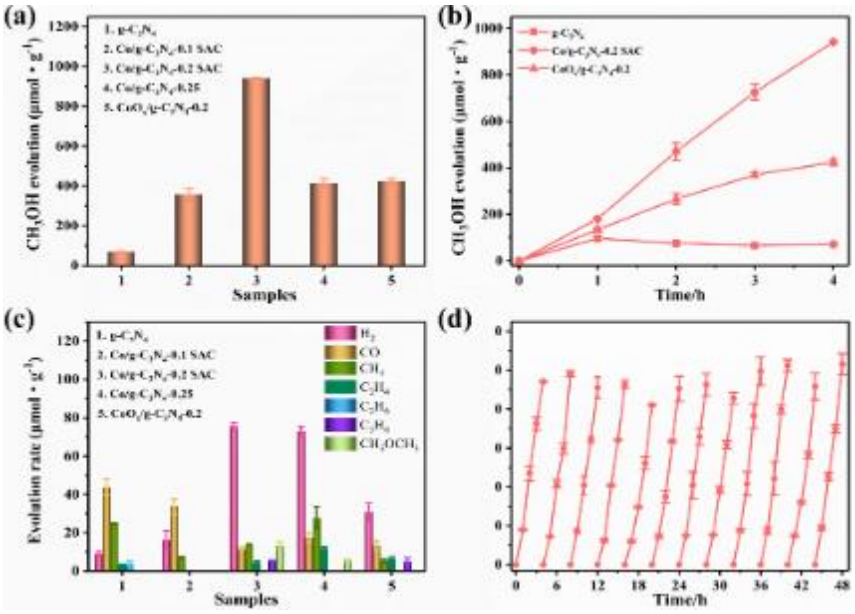

Fig. 4. Photocatalytic activity measurements from photoreduction of CO_2 with H_2O. (a) CH_3OH production and (c) H_2, CO, CH_4, C_2H_4, C_2H_6, C_3H_6, CH_3OCH_3 products at 4 hours over g-C_3N_4, Co/g-C_3N_4-0.1 SAC, Co/g-C_3N_4-0.2 SAC, Co/g-C_3N_4-0.25, and CoO_x/g-C_3N_4-0.2; Typical time profile of CH_3OH generation (b) by g-C_3N_4, Co/g-C_3N_4-0.2 SAC, and CoO_x/g-C_3N_4-0.2; (d) CH_3OH production corresponding to cycle experiments of Co/g-C_3N_4-0.2 SAC. Conditions: 5 mg of catalyst; CO_2 =4 ml, Ar as the balance gas; 300 W Xe lamp light source; Reactor volume: ca. 270 ml.

3.4 Mechanism of photocatalytic CO_2 reduction

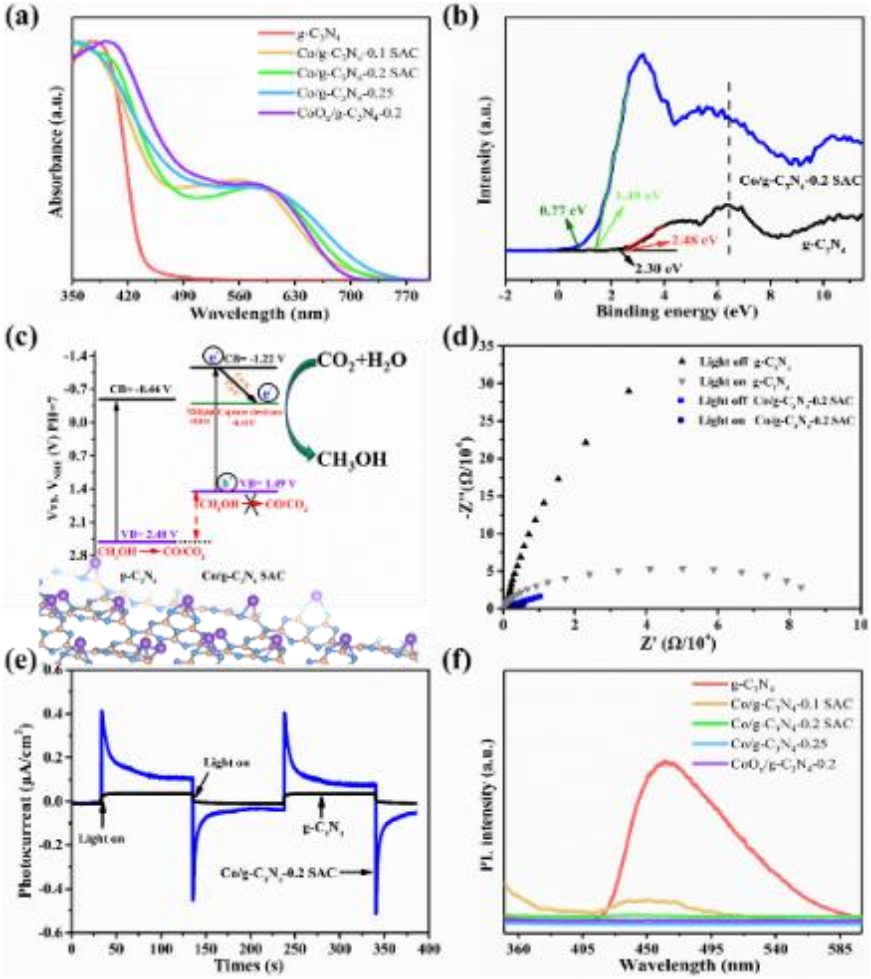

Fig. 5. (a) UV-vis diffuse reflectance spectra of g-C_3N_4, Co/g-C_3N_4-0.1 SAC, Co/g-C_3N_4-0.2 SAC, Co/g-C_3N_4-0.25, and CoO_x/g-C_3N_4-0.2; (b) XPS valence band spectra of the g-C_3N_4 and the Co/g-C_3N_4-0.2 SAC; (c) Band structure of g-C_3N_4 and Co/g-C_3N_4-0.2 SAC; (d) Time-dependent photocurrent curves (i-t curve) of g-C_3N_4 and Co/g-C_3N_4-0.2 SAC, and (e) corresponding electrochemical impedance spectroscopy (EIS) Nyquist plots; (f) Photoluminescence spectra of g-C_3N_4, Co/g-C_3N_4-0.1 SAC, Co/g-C_3N_4-0.2 SAC, Co/g-C_3N_4-0.25, and CoO_x/g-C_3N_4-0.2.

To unveil the reason why the ultrahigh density of single dispersed Co-N_2C active sites on Co/g-C_3N_4-0.2 SAC can reduce CO_2 to methanol with high activity and high

selectivity one can study the following three aspects: (a) light absorption ability; (b) generation ability and transfer efficiency of photogenerated carriers; (c) surface reaction [23, 62, 63]. The introduction of high loading monodispersed Co-N_2C sites in the Co/g-C_3N_4-0.2 SAC increased the light absorption range from 450 nm to 700 nm as compared with the g-C_3N_4 (**Fig. 5a**). The color of the Co/g-C_3N_4-0.2 SAC was light green and very different from the color of the g-C_3N_4 (**Fig. S9e**). The intense color resembles molecular systems like metal phthalocyanine or metal$(bpy)_3Cl_2$ [64, 65], further illustrating the strong interaction between single dispersed Co-N_2C active sites and g-C_3N_4 via Co-N and Co-C bonds. Although the Co/g-C_3N_4-0.1 SAC, Co/g-C_3N_4-0.2 SAC, Co/g-C_3N_4-0.25, and CoO_x/g-C_3N_4-0.2 have almost the similar light absorption ability (**Fig. 5a**), the photocatalytic activities were not as high as that of Co/g-C_3N_4-0.2 SAC (**Fig. 4a**). This suggested that the Co/g-C_3N_4-0.2 SAC with high activity and high selectivity for photocatalytic reduction of CO_2 to methanol was not mainly caused by its ultra-high density of single dispersed Co-N_2C active sites with enhanced light absorption ability.

The XPS valence band spectra (VBS) were analyzed to study the change of charge density (**Fig. 5b)**, the VBS of Co/g-C_3N_4-0.2 SAC showed two significantly different features as compared to that of g-C_3N_4. On the one hand, the peak at 6 eV, primarily ascribed to N 2p states was less sharp than that of g-C_3N_4. On the other hand, the band tail was prolonged to 0.77 eV, which was 1.53 eV lower than the band tail of g-C_3N_4 (2.30 eV). These features could be ascribed to the ultrahigh density of single dispersed Co-N_2C active sites and they strongly interact with g-C_3N_4 on the sample of Co/g-C_3N_4-

0.2 SAC. DFT calculations were conducted to analyze the effect of the ultrahigh density of single dispersed Co-N_2C sites on the local electronic density of g-C_3N_4. The charge transfer from single dispersed Co atoms to g-C_3N_4 was as high as 0.74 e^- based on the population analysis. As a result, there was an increased charge density on C and N atoms around cobalt atoms on Co/g-C_3N_4-0.2 SAC, consistent with the XPS analysis (**Fig. 1c-d**). This result indicated that an electron channel could be formed between cobalt atoms and g-C_3N_4 by Co-N and Co-C bonds at single dispersed Co-N_2C active sites, which would be conducive to the transmission of photogenerated carriers.

The valence band of g-C_3N_4 and Co/g-C_3N_4-0.2 SAC was mainly formed by the N 2p and a small fraction of C 2p, the conduction band was mainly formed by C 2p and Co 2p [66]. The valence band maximum (VBM) and conduction band minimum(CBM) of Co/g-C_3N_4-0.2 SAC (1.49 eV, -0.44 eV) moved up 0.99 and 0.78 as compared to that of g-C_3N_4 (2.48 eV, -1.22 eV), respectively(**Fig. 5b-c and Fig. S20)**, leading to much higher charge density at carbon atoms and nitrogen atoms in Co/g-C_3N_4-0.2 SAC. Although the band-gap of the Co/g-C_3N_4-0.2 SAC was significantly narrowed after the introduction of the ultrahigh density of single dispersed Co-N_2C active sites, it still matched redox potentials of CO_2/CH_4 (-0.24 V vs NHE) and CO_2/CH_3OH (-0.38 V vs NHE) [2]. Therefore, the ultrahigh density of single dispersed Co-N_2C active sites changes the band structure of g-C_3N_4 in the sample of Co/g-C_3N_4-0.2 SAC (**Fig. 5b-c**). More importantly, the ultrahigh density of single dispersed Co-N_2C sites with the half-filled d electrons of Co^{2+} led to the formation of a mid-gap energy level in the Co/g-C_3N_4-0.2 SAC as shown in **Fig. 5c** [11, 67]. It can serve as an electron gathering center

to form a localized electron center [11]. Therefore, it is concluded that the ultrahigh density of single dispersed Co-N_2C sites allowed to tune the electronic structure of g-C_3N_4 to promote photoreduction CO_2 to CH_3OH with high selectivity and activity with suppressing methanol over oxidation to CO and CO_2 as presented in **Fig. 4b**.

Another key aspect that influences the photoreduction CO_2 activity is the generation ability and transfer efficiency of photogenerated carriers. Compared to the g-C_3N_4, Co/g-C_3N_4-0.2 SAC revealed the highest time-dependent photocurrent and the smallest diameter of semicircle arc at the light on or light off (**Fig. 5d-e**). In addition, the Co/g-C_3N_4-0.1 SAC, Co/g-C_3N_4-0.2 SAC, Co/g-C_3N_4-0.25, and CoO_x/g-C_3N_4-0.2 showed almost no PL peak as compared with g-C_3N_4 (**Fig. 5f**). Thus, these results indicate that the ultrahigh density of single dispersed Co-N_2C active sites in the Co/g-C_3N_4-0.2 SAC increase charge separation and transfer efficiency in the interfacial zone compared to g-C_3N_4 [11, 48, 68].

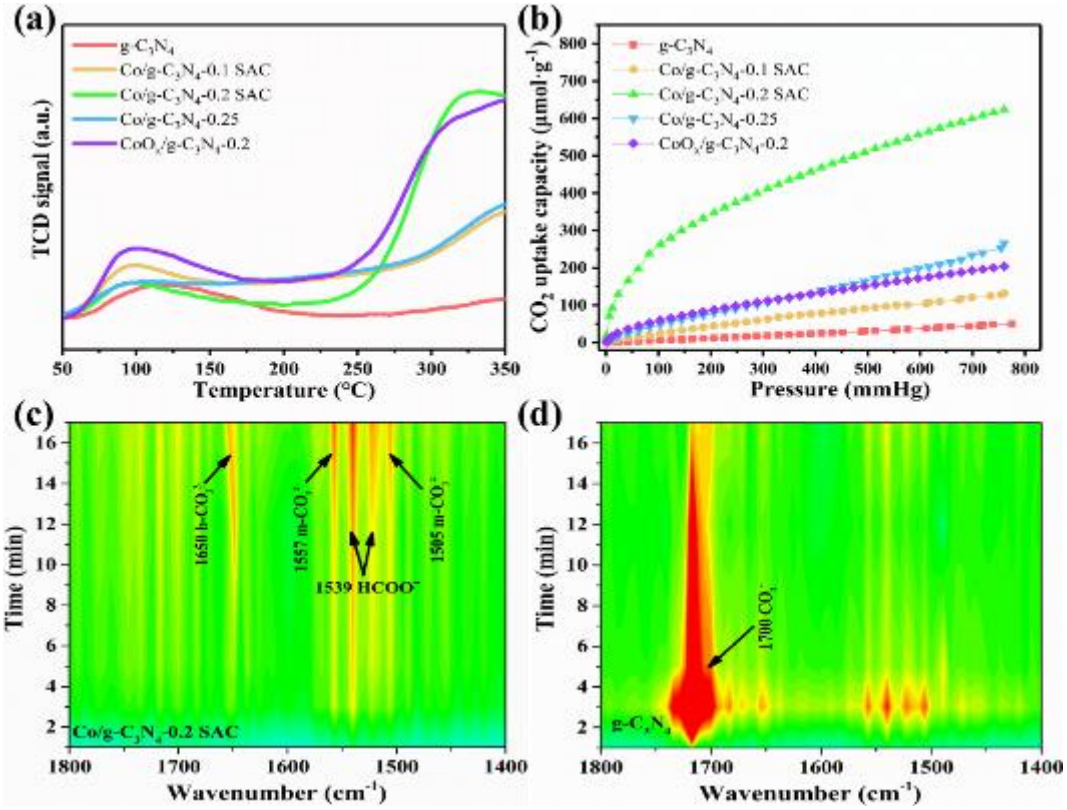

Fig. 6. (a) CO_2-TPD and (b) CO_2 adsorption isotherms of g-C_3N_4, Co/g-C_3N_4-0.1 SAC, Co/g-C_3N_4-0.2 SAC, Co/g-C_3N_4-0.25, and CoO_x/g-C_3N_4-0.2 samples, respectively; In situ DRIFTS spectra measured during photoreduction of CO_2 with H_2O after adsorption of saturated CO_2 and H_2O over (maxima (red) and minima (green)) on (c) Co/g-C_3N_4-0.2 SAC and (d) g-C_3N_4.

It is generally known that the adsorption of CO_2 on the photocatalyst surface is the first step of photocatalytic reduction of CO_2. The CO_2 adsorption capacity of Co/g-C_3N_4-0.2 SAC was 635.4 μmol g^{-1}, which was by a factor of 12, 4.8, 2.4 and 3.0 higher than that of g-C_3N_4 (51.9 μmol g^{-1}), Co/g-C_3N_4-0.1 SAC (131.8 μmol g^{-1}), Co/g-C_3N_4-0.25 (265.8 μmol g^{-1}) and CoO_x/g-C_3N_4-0.2 (208.8 μmol g^{-1}), respectively (**Fig. 6a**). The CO_2-TPD was also investigated to obtain more insights into CO_2 adsorption (**Fig.**

6b). After the introduction of the ultrahigh density of single dispersed Co-N_2C sites, the chemisorption (desorption peak at around 320 ℃) of CO_2 on Co/g-C_3N_4-0.1 SAC, Co/g-C_3N_4-0.2 SAC, Co/g-C_3N_4-0.25, and CoO_x/g-C_3N_4-0.2 was stronger than that on the g-C_3N_4. It indicated that Co species can improve the adsorption strength of CO_2 on the material surface. As presented in **Figure 6c-d**, the peaks of 1650 cm^{-1}, 1557 cm^{-1}, 1539 cm^{-1}, 1505 cm^{-1}, and 1700 cm^{-1} were assigned to bidentate carbonates (b-CO_3^{2-}), monodentate carbonates (m-CO_3^{2-}), formate species ($HCOO^-$), monodentate carbonates (m-CO_3^{2-}), and CO_2^-, respectively [69-73]. Interestingly, the normalization intensities of adsorbed b-CO_3^{2-} and m-CO_3^{2-} on the surface of Co/g-C_3N_4-0.2 SAC increased with the increase of the illumination time. This may be due to the local abundant electrons at the high density single dispersed Co-N_2C sites during illumination promoted the absorption of CO_2 on the surface of the Co/g-C_3N_4-0.2 SAC. Because high surface charge density contributes to enhancing CO_2 adsorption and activation [74, 75]. Therefore, the ultrahigh density of single dispersed Co-N_2C sites on Co/g-C_3N_4-0.2 SAC contributed to improving CO_2 adsorption and activation ability, thereby promoting the highly selective and activity photocatalytic reduction of CO_2 to methanol.

All in all, high density of single dispersed Co-N_2C active sites on the sample of Co/g-C_3N_4-0.2 SAC played a critical role in photocatalytic CO_2 reduction to CH_3OH with high activity and high selectivity due to improving CO_2 adsorption and activation ability during the photoreduction CO_2 process and enhancing the photogenerated electron-hole pair separation efficiency. More importantly, the high density of single dispersed Co-N_2C sites can serve as the electron gathering centers to localize

photogenerated electrons and tune the band structure of g-C_3N_4 to boost the photoreduction CO_2 to methanol and suppress the methanol overoxidation. In addition, the high thermal stability of the Co/g-C_3N_4-0.2 SAC structure was a key factor for maintaining the high stability of photoreduction CO_2 to methanol.

4 Conclusion

In summary, we have proposed a novel pyrolysis-induced-vaporization strategy for the fabrication of Co/g-C_3N_4 SACs with ultrahigh surface metal loading of 24.6 wt%. Such high surface loading of single Co atoms was achieved using g-C_3N_4 NSs as the substrate, because it can offer numerous uniform coordination N_2C sites for Co-anchoring, followed by the two-step calcination to suppress the Co aggregation during the calcination process. The formation of the ultrahigh density of single dispersed Co-N_2C active sites promoted the migration of photogenerated carriers and helps for the localization of photogenerated electrons under light irradiation. As a result, Co/g-C_3N_4 SAC was found to be beneficial for photocatalytic CO_2 reduction to CH_3OH with high activity, high selectivity, and high stability. This work opens a new opportunity for fabricating ultrahigh surface cobalt density SACs, which can be used for diverse applications such as photocatalysis, electrocatalysis, and photoelectrocatalysis.

Declaration of Competing Interest

The authors declare that they have no known competing financial interests or personal relationships that could have appeared to influence the work reported in this paper.

Acknowledgments

This research was financially supported by the Sichuan Provincial International Cooperation Project (2019YFH0164; 2021YFH0055), the Cheung Kong Scholars Program of China. We would like to thank the Institute for Beam Physics and Technology (IBPT) for the operation of the storage ring, the Karlsruhe Research Accelerator (KARA). We acknowledge the KIT light source for the provision of instruments at the CAT-ACT beamline of the Institute of Catalysis Research and Technology (IKFT), in particular, Dr. Tim Prüßmann and Dr. Anna Zimina (IKFT) for their help and technical support during experiments. We appreciate the calculation support from the National Supercomputing Center in Shenzhen.

Appendix A. Supplementary data

Supplementary data associated with this article can be found in the online version.

References

[1] T.H. Tan, B. Xie, Y.H. Ng, S.F.B. Abdullah, H.Y.M. Tang, N. Bedford, R.A. Taylor, K.-F. Aguey-Zinsou, R. Amal, J. Scott, Nat. Catal. 3 (2020) 1034-1043.
[2] D. Adekoya, M. Tahir, N.A.S. Amin, Sust. Energ. Rev. 116 (2019) 109389.
[3] X. Jiang, X. Nie, X. Guo, C. Song, J.G. Chen, Chem. Rev. 120 (2020) 7984-8034.
[4] C.H. Li, X. Tong, P. Yu, W. Du, J. Wu, H. Rao, Z.M.M. Wang, J. Mater. Chem. A 7 (2019) 16622-16642.
[5] S. Ning, H. Xu, Y. Qi, L. Song, Q. Zhang, S. Ouyang, J. Ye, ACS Catal. 10 (2020) 4726-4736.
[6] K.K. Mandari, J.Y. Do, A.K.R. Police, M. Kang, Appl. Catal. B: Enviorn. 231 (2018) 137-150.
[7] Y. Cao, S. Chen, Q. Luo, H. Yan, Y. Lin, W. Liu, L. Cao, J. Lu, J. Yang, T. Yao, S. Wei, Angew. Chem. Int. Ed. 56 (2017) 12191-12196.
[8] S.K. Kaiser, Z. Chen, D. Faust Akl, S. Mitchell, J. Perez-Ramirez, Chem. Rev. 120 (2020) 11703-11809.
[9] C. Gao, S. Chen, Y. Wang, J. Wang, X. Zheng, J. Zhu, L. Song, W. Zhang, Y. Xiong, Adv. Mater. 30 (2018) e1704624.
[10] K. Kim, T. Kang, M. Kim, J. Kim, Appl. Catal. B: Enviorn. 275 (2020) 119107.
[11] W. Liu, L. Cao, W. Cheng, Y. Cao, X. Liu, W. Zhang, X. Mou, L. Jin, X. Zheng, W. Che, Q. Liu, T. Yao, S. Wei, Angew. Chem. Int. Ed. 56 (2017) 9312-9317.
[12] Y. Zheng, Y. Jiao, Y. Zhu, Q. Cai, A. Vasileff, L.H. Li, Y. Han, Y. Chen, S.Z. Qiao, J. Am. Chem. Soc. 139 (2017) 3336-3339.
[13] X. Jiang, X. Nie, X. Guo, C. Song, J.G. Chen, Chem. Rev. 120 (2020) 7984-8034.
[14] X. Wang, Y. Wang, M. Gao, J. Shen, X. Pu, Z. Zhang, H. Lin, X. Wang, Appl. Catal. B: Enviorn. 270 (2020) 118876.
[15] G. Wang, C.T. He, R. Huang, J. Mao, D. Wang, Y. Li, J. Am. Chem. Soc. 142 (2020) 19339-19345.

[16] P. Huang, J. Huang, S.A. Pantovich, A.D. Carl, T.G. Fenton, C.A. Caputo, R.L. Grimm, A.I. Frenkel, G. Li, J. Am. Chem. Soc. 140 (2018) 16042-16047.
[17] X. Xiao, L. Zhang, H. Meng, B. Jiang, H. Fu, Solar RRL 5(2020) 2000609.
[18] L. Zhao, Y. Zhang, L.B. Huang, X.Z. Liu, Q.H. Zhang, C. He, Z.Y. Wu, L.J. Zhang, J. Wu, W. Yang, L. Gu, J.S. Hu, L.J. Wan, Nat. Commun. 10 (2019) 1278.
[19] Y. Xiong, W. Sun, Y. Han, P. Xin, X. Zheng, W. Yan, J. Dong, J. Zhang, D. Wang, Y. Li, Nano Res. 14 (2021) 2418-2423.
[20] S. Ji, Y. Qu, T. Wang, Y. Chen, G. Wang, X. Li, J. Dong, Q. Chen, W. Zhang, Z. Zhang, S. Liang, R. Yu, Y. Wang, D. Wang, Y. Li, Angew. Chem. Int. Ed. 59 (2020) 10651-10657.
[21] Y. Xiong, W.M. Sun, P.Y. Xin, W.X. Chen, X.S. Zheng, W.S. Yan, L.R. Zheng, J.C. Dong, J. Zhang, D.S. Wang, Y.D. Li, Adv. Mater. 32 (2020) e2000896.
[22] P. Chen, B. Lei, X. Dong, H. Wang, J. Sheng, W. Cui, J. Li, Y. Sun, Z. Wang, F. Dong, ACS nano 14 (2020) 15841-15852.
[23] R.Y. Zhang, P.H. Li, F. Wang, L.Q. Ye, A. Gaur, Z.A. Huang, Z.Y. Zhao, Y. Bai, Y. Zhou, Appl. Catal. B: Enviorn. 250 (2019) 273-279.
[24] X. Wang, K. Maeda, A. Thomas, K. Takanabe, G. Xin, J.M. Carlsson, K. Domen, M. Antonietti, Nat. mate. 8 (2009) 76-80.
[25] Z. Zhou, J. Wang, J. Yu, Y. Shen, Y. Li, A. Liu, S. Liu, Y. Zhang, J. Am. Chem. Soc. 137 (2015) 2179-2182.
[26] A. Zimina, K. Dardenne, M.A. Denecke, D.E. Doronkin, E. Huttel, H. Lichtenberg, S. Mangold, T. Pruessmann, J. Rothe, T. Spangenberg, R. Steininger, T. Vitova, H. Geckeis, J.D. Grunwaldt, Rev. Sci. Instrum. 88 (2017) 113113.
[27] B. Ravel, M. Newville, J. Synchrotron Radiat. 12 (2005) 537-541.
[28] Z.M. Xia, H. Zhang, K.C. Shen, Y.Q. Qu, Z. Jiang, Physica B 542 (2018) 12-19.
[29] B. Tan, Y. Ye, Z. Huang, L. Ye, M. Ma, Y. Zhou, Chinese Chem. Lett. 31 (2020) 1530-1534.
[30] Y. Cao, L. Guo, M. Dan, D.E. Doronkin, C. Han, Z. Rao, Y. Liu, J. Meng, Z. Huang, K. Zheng, P. Chen, F. Dong, Y. Zhou, Nat. Commun. 12 (2021).
[31] Y. Cao, R. Zhang, T. Zhou, S. Jin, J. Huang, L. Ye, Z. Huang, F. Wang, Y. Zhou, ACS Appl. Mater. Inter. 12 (2020) 9935-9943.
[32] Z. Rao, Y. Cao, Z. Huang, Z. Yin, W. Wan, M. Ma, Y. Wu, J. Wang, G. Yang, Y. Cui, Z. Gong, Y. Zhou, ACS Catal. 11 (2021) 4730-4738.
[33] B.C. Zhu, J.F. Zhang, C.J. Jiang, B. Cheng, J.G. Yu, Appl. Catal. B: Enviorn. 207 (2017) 27-34.
[34] F. Raziq, A. Hayat, M. Humayun, S.K. Baburao Mane, M.B. Faheem, A. Ali, Y. Zhao, S. Han, C. Cai, W. Li, D.-C. Qi, J. Yi, X. Yu, M.B.H. Breese, F. Hassan, F. Ali, A. Mavlonov, K. Dhanabalan, X. Xiang, X. Zu, S. Li, L. Qiao, Appl. Catal. B: Enviorn. 270 (2020) 118867.
[35] B.C. Zhu, L.Y. Zhang, D.F. Xu, B. Cheng, J.G. Yu, J. CO_2 Util. 21 (2017) 327-335.
[36] G. Zhang, S. Zang, L. Lin, Z.A. Lan, G. Li, X. Wang, ACS Appl. Mater. Inter. 8 (2016) 2287-2296.
[37] R.Y. Zhang, M.Z. Ma, Q. Zhang, F. Dong, Y. Zhou, Appl. Catal. B: Enviorn. 235

(2018) 17-25.
[38] H. Yu, R. Shi, Y. Zhao, T. Bian, Y. Zhao, C. Zhou, G.I.N. Waterhouse, L.Z. Wu, C.H. Tung, T. Zhang, Adv. Mater. 29 (2017) 1605148.
[39] H. Yu, L. Shang, T. Bian, R. Shi, G.I. Waterhouse, Y. Zhao, C. Zhou, L.Z. Wu, C.H. Tung, T. Zhang, Adv. Mater. 28 (2016) 5080-5086.
[40] W. Wang, Y. Huang, Z. Wang, Acta Phys. Chim. Sin. 0 (2020) 2011073-2011070.
[41] F. Yu, L. Wang, Q. Xing, D. Wang, X. Jiang, G. Li, A. Zheng, F. Ai, J.-P. Zou, Chinese Chem. Lett. 31 (2020) 1648-1653.
[42] J. Ge, L. Zhang, J. Xu, Y. Liu, D. Jiang, P. Du, Chinese Chem. Lett. 31 (2020) 792-796.
[43] P.W. Chen, K. Li, Y.X. Yu, W.D. Zhang, Appl. Surf. Sci. 392 (2017) 608-615.
[44] A.Y. Makoto Yuasa, K.T. Hisayuki Itsuki, a.K.O. Masakuni Yamamoto, Chem. Mater. 17 (2005) 4278-4281.
[45] T.L. Feng, Q.S. Zeng, S.Y. Lu, M.X. Yang, S.Y. Tao, Y.X. Chen, Y. Zhao, B. Yang, ACS Sustain. Chem. Eng. 7 (2019) 7047-7057.
[46] G. Zhang, C. Huang, X. Wang, Small 11 (2015) 1215-1221.
[47] X. Rong, H.J. Wang, X.L. Lu, R. Si, T.B. Lu, Angew. Chem. Int. Ed. 59 (2020) 1961-1965.
[48] Y. Cao, S. Chen, Q. Luo, H. Yan, Y. Lin, W. Liu, L. Cao, J. Lu, J. Yang, T. Yao, S. Wei, Angew. Chem. Int. Ed. 56 (2017) 12191-12196.
[49] J.B. Wu, H. Zhou, Q. Li, M. Chen, J. Wan, N.A. Zhang, L.K. Xiong, S. Li, B.Y. Xia, G. Feng, M.L. Liu, L. Huang, Adv. Energy Mater. 9 (2019).
[50] J.B. Wu, L.K. Xiong, B.T. Zhao, M.L. Liu, L. Huang, Small Methods 4 (2020) 1900540.
[51] S.P. Ding, M.J. Hulsey, J. Perez-Ramirez, N. Yang, Joule 3 (2019) 2897-2929.
[52] X. Du, G. Zou, Z. Wang, X. Wang, Nanoscale 7 (2015) 8701-8706.
[53] Y.G. Xu, M. Xie, S.Q. Huang, H. Xu, H.Y. Ji, J.X. Xia, Y.P. Li, H.M. Li, RSC Adv. 5 (2015) 26281-26290.
[54] H.J. Yan, X.H. Xie, K.W. Liu, H.M. Cao, X.J. Zhang, Y.L. Luo, Powder Technol. 221 (2012) 199-202.
[55] T. Cseri, S. Békássy, G. Kenessey, G. Liptay, F. Figueras, Thermochimica Acta 288 (1996) 137-154.
[56] Y.T. Qu, Z.J. Li, W.X. Chen, Y. Lin, T.W. Yuan, Z.K. Yang, C.M. Zhao, J. Wang, C. Zhao, X. Wang, F.Y. Zhou, Z.B. Zhuang, Y. Wu, Y.D. Li, Nat. Catal. 1 (2018) 781-786.
[57] S. Shwan, M. Skoglundh, L.F. Lundegaard, R.R. Tiruvalam, T.V.W. Janssens, A. Carlsson, P.N.R. Vennestrøm, ACS Catal. 5 (2014) 16-19.
[58] L. He, W. Zhang, S. Liu, Y. Zhao, Appl. Catal. B: Enviorn. 298 (2021) 120546.
[59] G.X. Zhao, H. Pang, G.G. Liu, P. Li, H.M. Liu, H.B. Zhang, L. Shi, J.H. Ye, Appl. Catal. B: Enviorn. 200 (2017) 141-149.
[60] J. Zhou, W. Chen, C. Sun, L. Han, C. Qin, M. Chen, X. Wang, E. Wang, Z. Su, ACS Appl. Mater. Inter. 9 (2017) 11689-11695.
[61] P. Sharma, S. Kumar, O. Tomanec, M. Petr, J. Zhu Chen, J.T. Miller, R.S. Varma, M.B. Gawande, R. Zboril, Small 17 (2021) e2006478.

[62] L.J. Fang, X.L. Wang, Y.H. Li, P.F. Liu, Y.L. Wang, H.D. Zeng, H.G. Yang, Appl. Catal. B: Enviorn. 200 (2017) 578-584.
[63] D.M. Schultz, T.P. Yoon, Science 343 (2014) 1239176.
[64] C. Gao, Q. Meng, K. Zhao, H. Yin, D. Wang, J. Guo, S. Zhao, L. Chang, M. He, Q. Li, H. Zhao, X. Huang, Y. Gao, Z. Tang, Adv. Mater. 28 (2016) 6485-6490.
[65] S.N. Talapaneni, G. Singh, I.Y. Kim, K. AlBahily, A.H. Al-Muhtaseb, A.S. Karakoti, E. Tavakkoli, A. Vinu, Adv. Mater. (2019) e1904635.
[66] C. Feng, L. Tang, Y. Deng, J. Wang, Y. Liu, X. Ouyang, H. Yang, J. Yu, J. Wang, Appl. Catal. B: Enviorn. 281 (2021) 119539.
[67] Z. Teng, Q. Zhang, H. Yang, K. Kato, W. Yang, Y.-R. Lu, S. Liu, C. Wang, A. Yamakata, C. Su, B. Liu, T. Ohno, Nat. Catal. 4 (2021) 374-384.
[68] Q.Q. Song, J.Q. Li, L. Wang, Y. Qin, L.Y. Pang, H. Liu, J. Catal. 370 (2019) 176-185.
[69] L. Liu, H. Zhao, J.M. Andino, Y. Li, ACS Catal. 2 (2012) 1817-1828.
[70] C. Han, R. Zhang, Y. Ye, L. Wang, Z. Ma, F. Su, H. Xie, Y. Zhou, P.K. Wong, L. Ye, J. Mater. Chem. A 7 (2019) 9726-9735.
[71] M.M. Millet, G. Algara-Siller, S. Wrabetz, A. Mazheika, F. Girgsdies, D. Teschner, F. Seitz, A. Tarasov, S.V. Levchenko, R. Schlogl, E. Frei, J. Am. Chem. Soc. 141 (2019) 2451-2461.
[72] S. Neatu, J.A. Macia-Agullo, P. Concepcion, H. Garcia, J. Am. Chem. Soc. 136 (2014) 15969-15976.
[73] N. Ojha, A. Bajpai, S. Kumar, Catal. Sci. Technol. 9 (2019) 4598-4613.
[74] N.N. Vu, S. Kaliaguine, T.O. Do, Adv. Funct. Mater. 29 (2019) 1901825.
[75] X. Li, Y. Sun, J. Xu, Y. Shao, J. Wu, X. Xu, Y. Pan, H. Ju, J. Zhu, Y. Xie, Nat. Energy 4 (2019) 690-699.

Supplementary Information

Ultrahigh surface density of Co-N_2C single-atom-sites for boosting photocatalytic CO_2 reduction to methanol

Minzhi Ma[a, b], Zeai Huang*[a, b], Dmitry E. Doronkin[c], Wenjun Fa[d], Zhiqiang Rao[b], Yanzhao Zou[b], Rui Wang[b], Yunqian Zhong[b], Yuehan Cao[b], Ruiyang Zhang[b], and Ying Zhou*[a, b]

[a] State Key Laboratory of Oil and Gas Reservoir Geology and Exploitation, Southwest Petroleum University Chengdu, 610500, China

E-mail: zeai.huang@swpu.edu.cn, yzhou@swpu.edu.cn

Fax: +86 28 83037406; Tel: +86 28 83037411

[b] School of New Energy and Materials, Southwest Petroleum University Chengdu, 610500, China

[c] Institute of Catalysis Research and Technology and Institute for Chemical Technology and Polymer Chemistry, Karlsruhe Institute of Technology Karlsruhe, 76131, Germany

[d] Key Laboratory of Micro-Nano Materials for Energy Storage and Conversion of Henan Province & College of Advanced Materials and Energy, Xuchang University Henan, 461000, China

* Corresponding author: Zeai Huang; Ying Zhou (zeai.huang@swpu.edu.cn, yzhou@swpu.edu.cn)

Table of contents

1.1 Morphology of samples

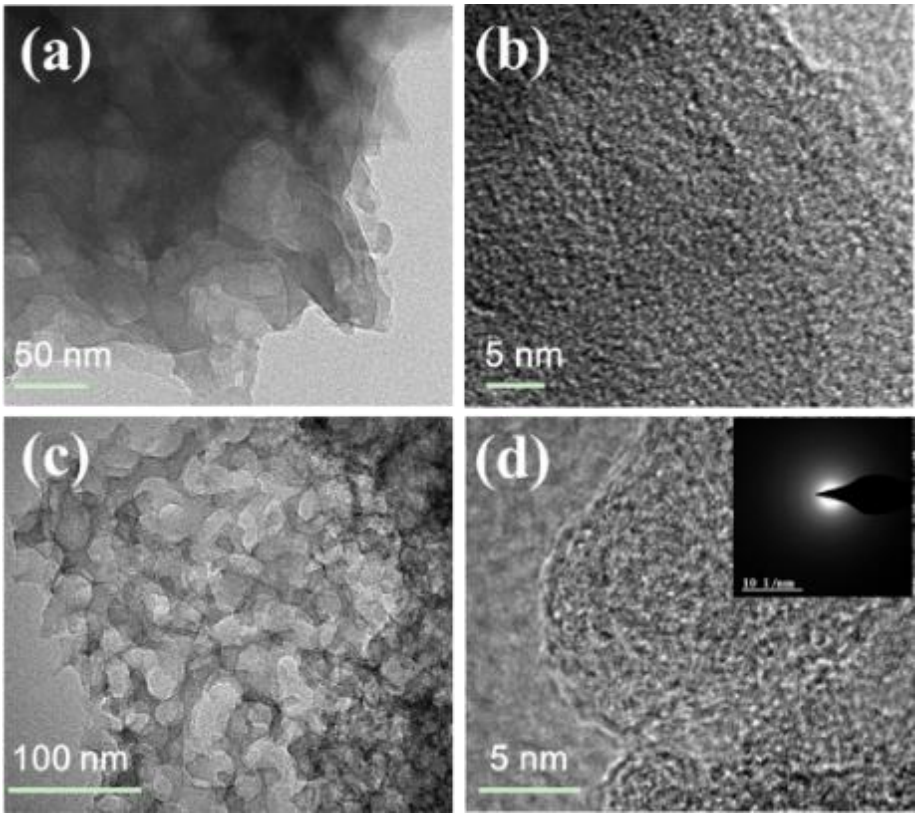

Figure S1. TEM (a,c) and HR-TEM (b, d) images of g-C_3N_4 and Co/g-C_3N_4-0.2

1.2 AC-HAADF-STEM image and EDX mapping

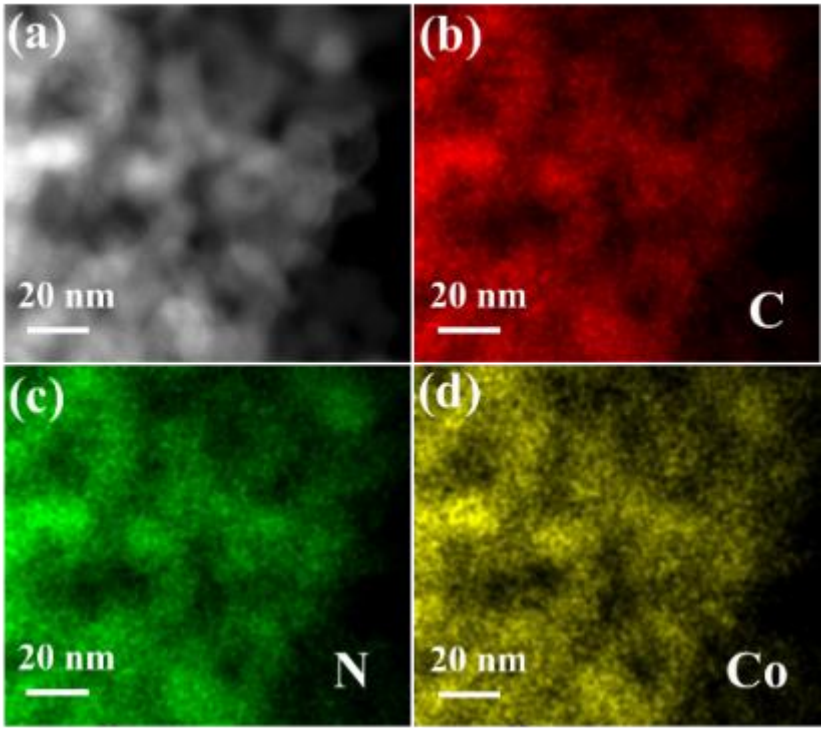

Figure S2. (a) AC-HAADF-STEM image and the corresponding EDX mapping of (b) carbon, (c) nitrogen, and (d) cobalt elements of Co/g-C_3N_4-0.2.

1.3 AC-HAADF-STEM image

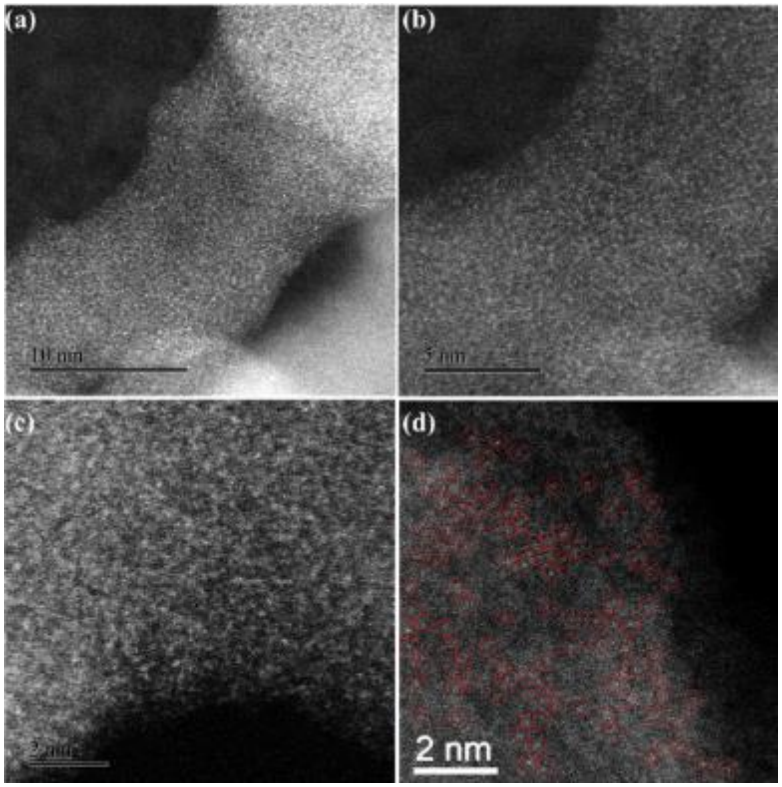

Figure S3. AC-HAADF-STEM image of Co/g-C_3N_4-0.2

1.4 EDX spectrum

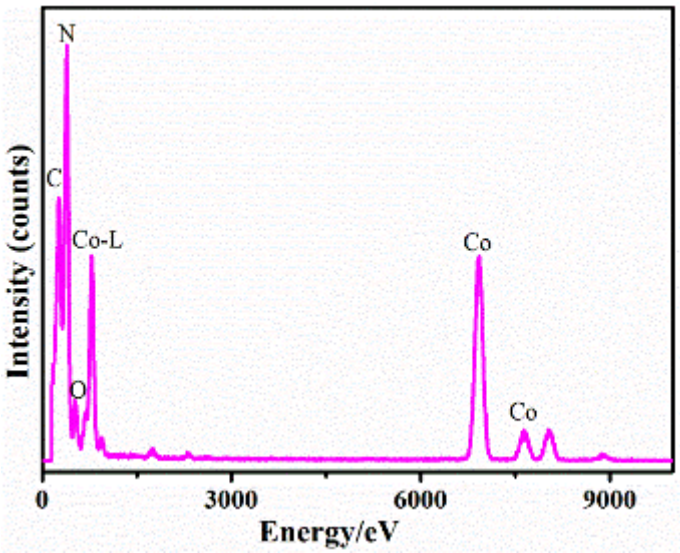

Figure S4. The EDX spectrum of Co/g-C_3N_4-0.2.

1.5 High-resolution Co 1s XPS spectrum

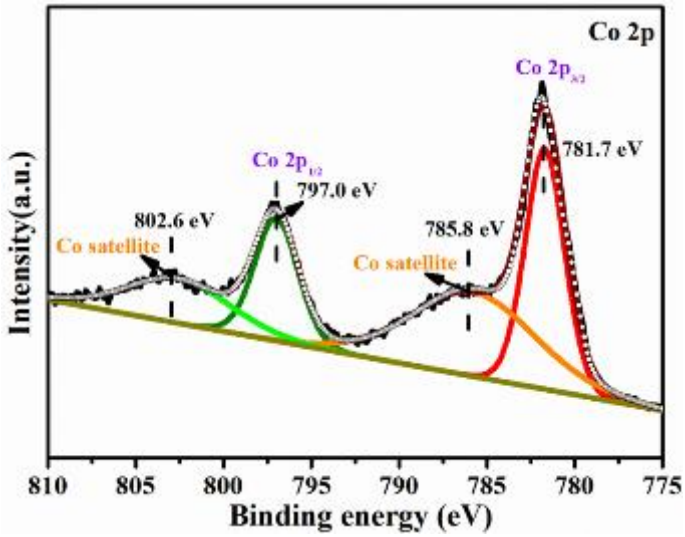

Figure S5. High-resolution Co 1s XPS spectrum of Co/g-C_3N_4-0.2.

1.6 XRD patterns of CoC_xN_y

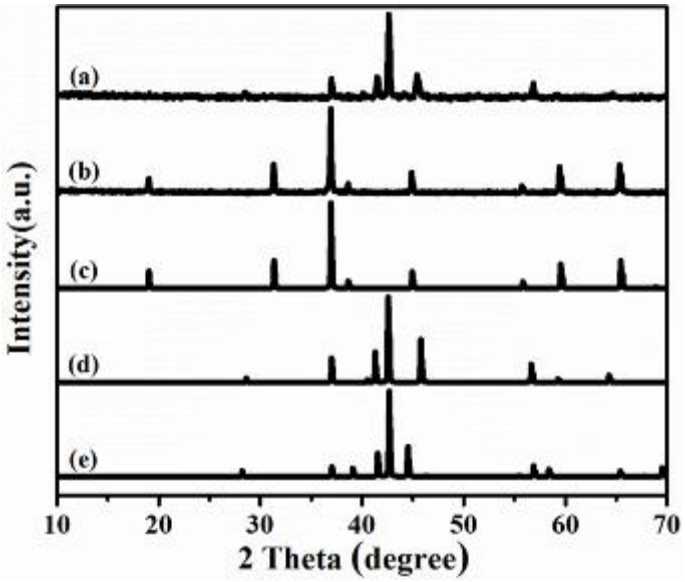

Figure S6. XRD patterns of (a) CoC_xN_y prepared by annealing the mixture of Co_3O_4 and g-C_3N_4-NSs at 550 °C for 1 h at Ar atmosphere, (b) commercial Co_3O_4, (c) Co_3O_4-JCPDS 74-1657 reference, (d) Co_2C-JCPDS 72-1369 reference, and (e) Co_2N-JCPDS 72-1368 reference, respectively.

1.7 EXAFS spectra

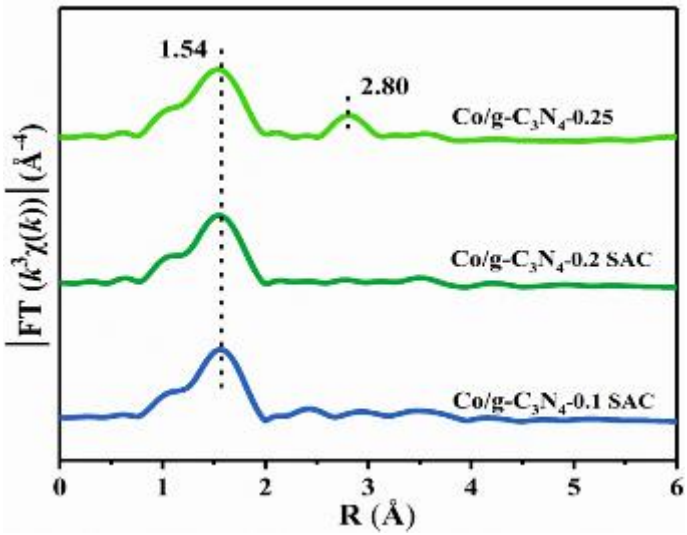

Figure S7. Fourier-transformed (FT) Co k^3-weighted EXAFS spectra (uncorrected for the phase shift) of Co/g-C_3N_4-0.1 SAC, Co/g-C_3N_4-0.2 SAC, and Co/g-C_3N_4-0.25.

1.8 The morphology of the samples

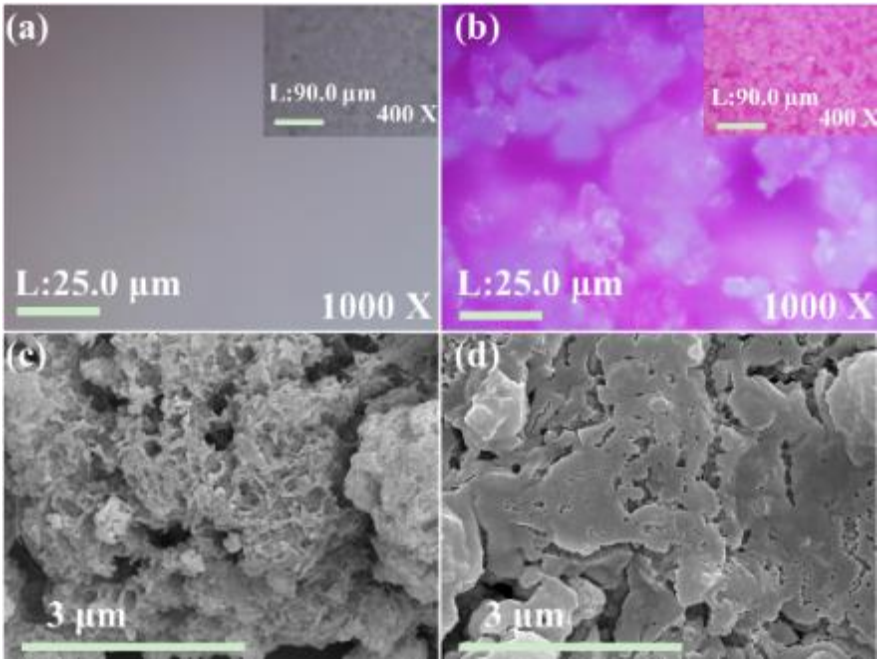

Figure S8. The optical images and SEM images of (a, c) g-C_3N_4-NSs and (b, d) the mixture of g-C_3N_4-NSs and $Co(NO_3)_2 \cdot 6H_2O$;

1.9 The color of the samples

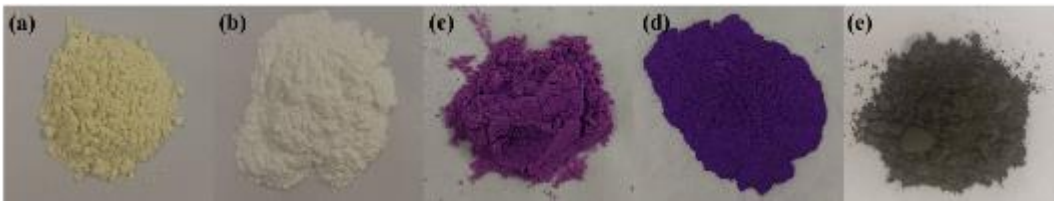

Figure S9. The color of the samples (a) g-C_3N_4, (b) g-C_3N_4-NSs, (c) the mixture of $Co(NO_3)_2 \cdot 6H_2O$ and g-C_3N_4-NSs, (d) the mixture of $Co(NO_3)_2 \cdot 6H_2O$ and g-C_3N_4-NSs after pre-drying at 130 ºC for 9 h, (e) Co/g-C_3N_4-0.2 SAC.

1.10 XRD patterns of bulk g-C_3N_4 and g-C_3N_4-NSs

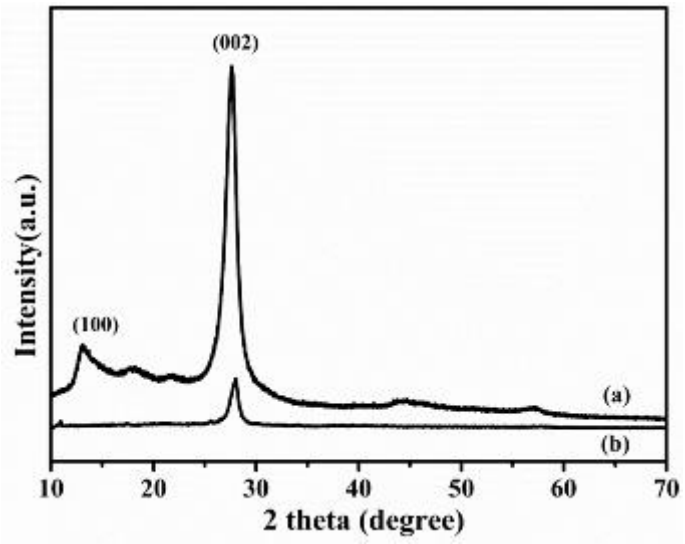

Figure S10. XRD patterns of (a) bulk g-C_3N_4, (b) g-C_3N_4-NSs.

1.11 XRD patterns of Co/bulk-g-C_3N_4-0.2

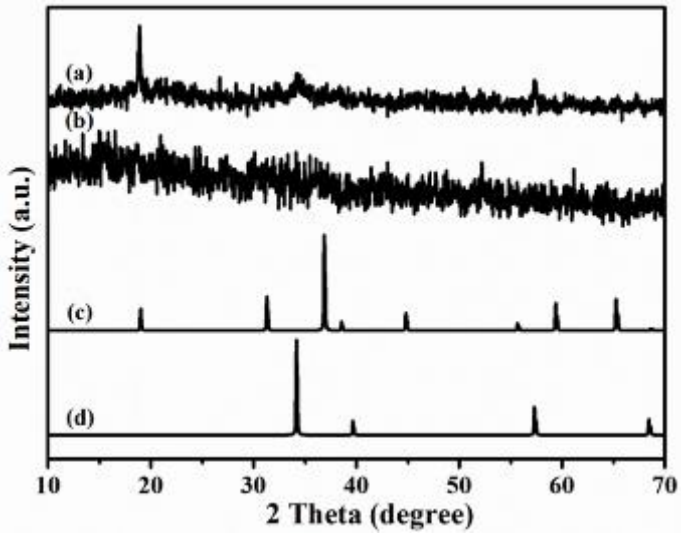

Figure S11. (a) The XRD patterns of (a) CoO_x/g-C_3N_4-0.2, (b) Co/g-C_3N_4-0.2 SAC, (c) Co_3O_4-JCPDS 42-1467, and (d) CoO-JCPDS 42-1300.

1.12 Color of the tube furnace after pyrolyzing

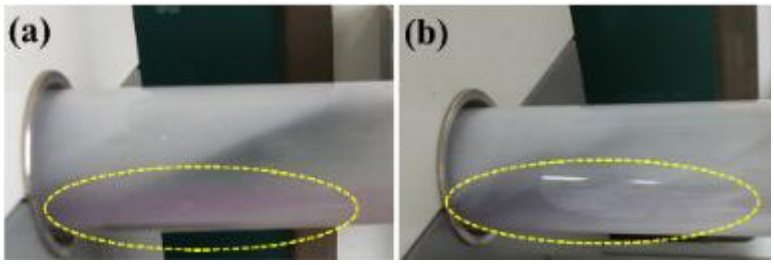

Figure S12. Color of the tube furnace after pyrolyzing the mixture of $Co(NO_3)_2 \cdot 6H_2O$ and g-C_3N_4-NSs (a) Co/g-C_3N_4-0.2 SACs prepared by two-step calcination, (b) m-Co/g-C_3N_4-0.2 prepared by one-step calcination.

1.13 The XRD patterns

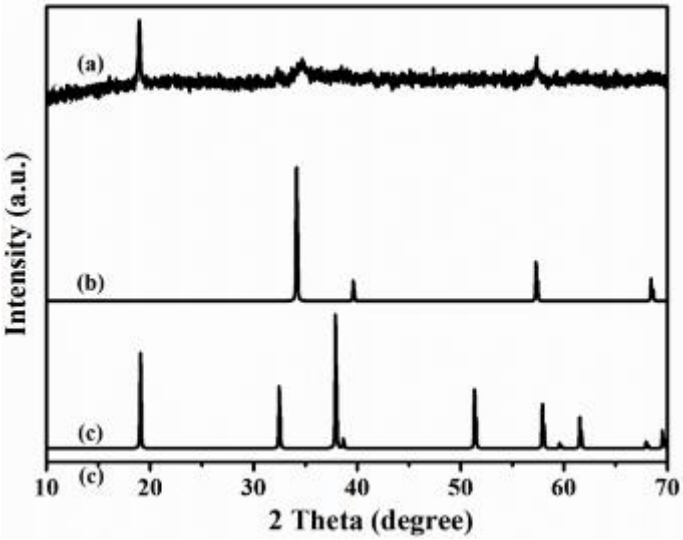

Figure S13. The XRD patterns of (a) Co/g-C_3N_4-0.2 prepared by one-step calcination without the pre-drying treatment process (130 ºC), (b) CoO-JCPDS 42-1300, and (c) $Co(OH)_2$-JCPDS 30-0443.

1.14 TG curve

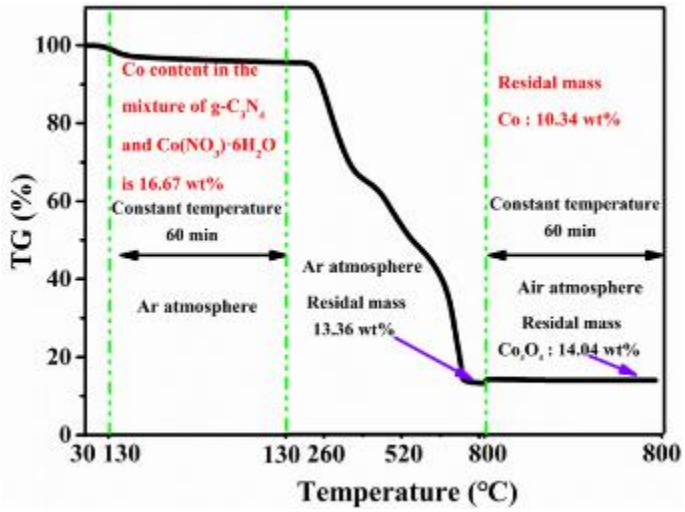

Figure S14. The TG curve of the mixture of g-C_3N_4-NSs and $Co(NO_3)_2 \cdot 6H_2O$.

1.15 TEM and HR TEM images

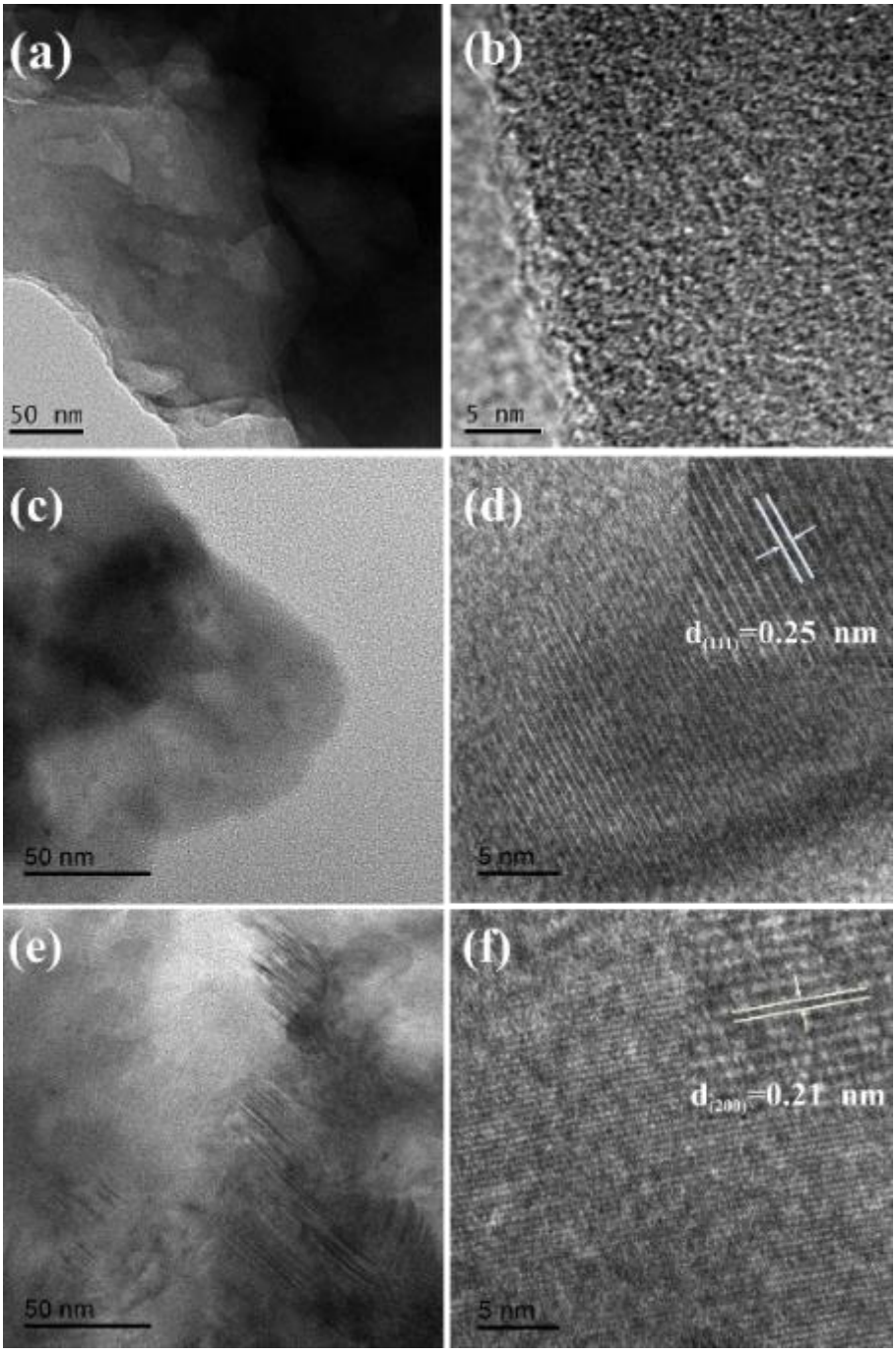

Figure S15. TEM (a, c, e) and HR-TEM (b, d, f) images of Co/g-C_3N_4-0.1 SAC, Co/g-C_3N_4-0.25, and CoO_x/g-C_3N_4-0.2.

1.16 Isotope experiment

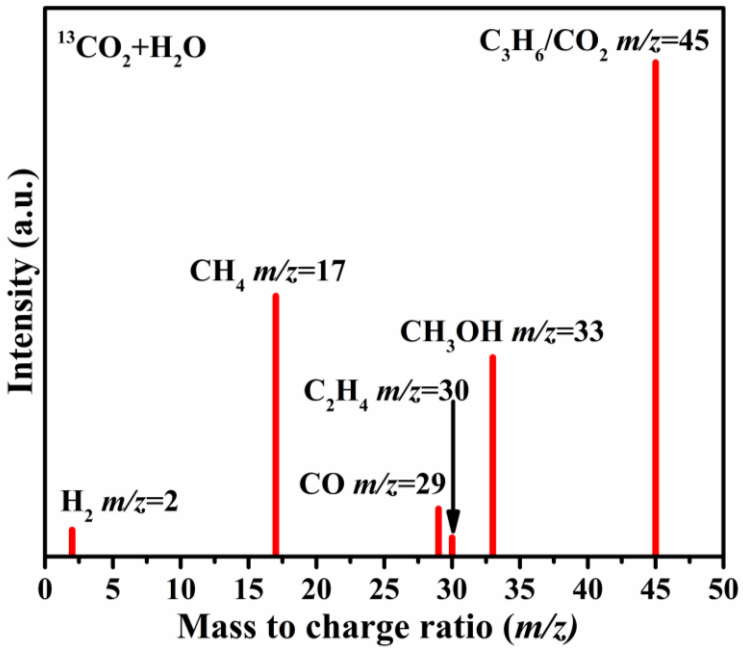

Figure S16. Mass spectra obtained during the photocatalytic conversion of $^{13}CO_2$ over Co/g-C_3N_4-0.2 SAC.

1.17 Recycle experiments

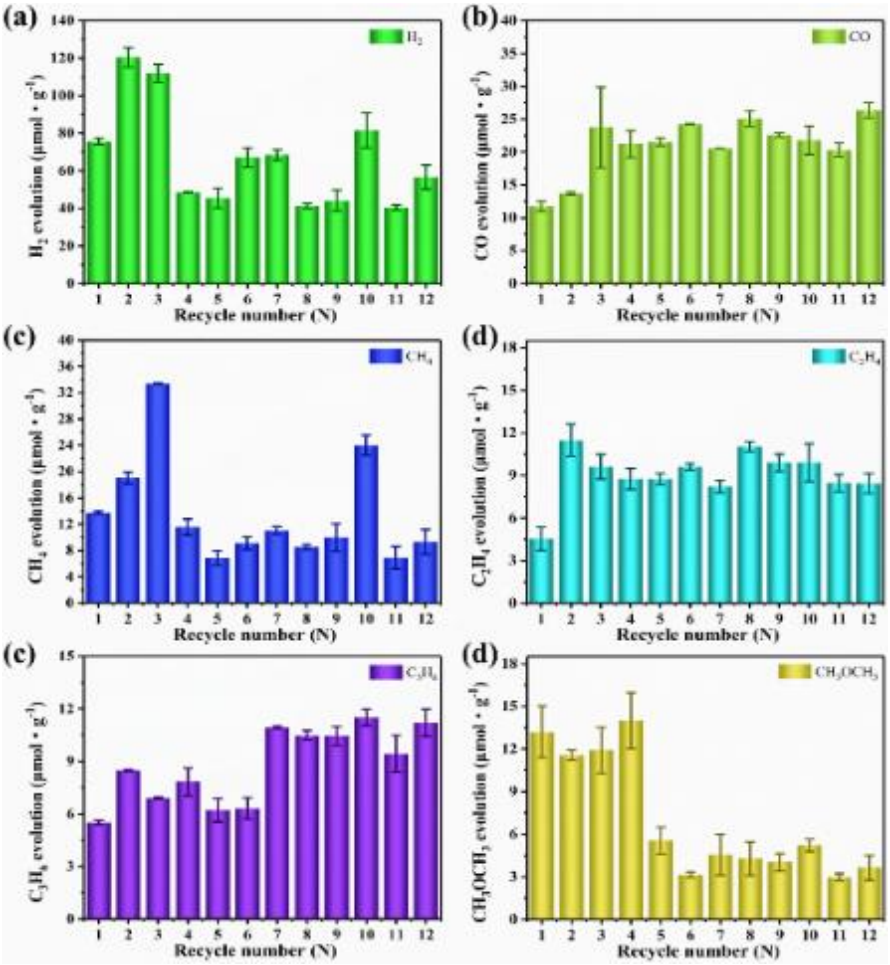

Figure S17. (a) H_2, (b) CO, (c) CH_4, (d) C_2H_4, (e) C_3H_6, and (f) CH_3OCH_3 production corresponding to cycle experiments of Co/g-C_3N_4-0.2 SAC.

1.18 Gas chromatographic signal

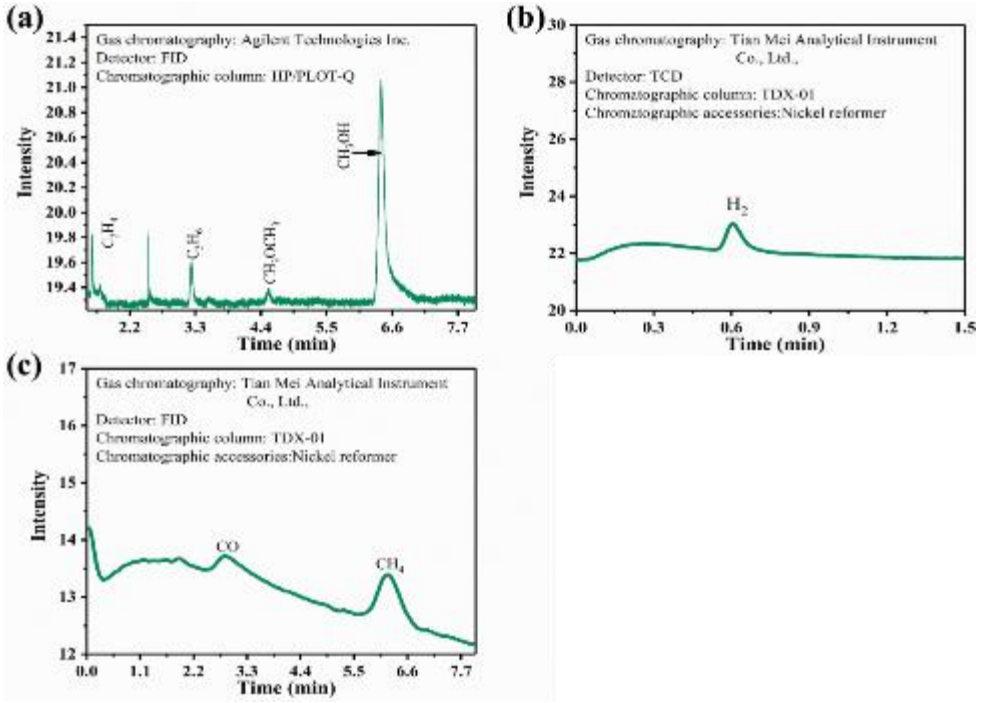

Figure S18. Results of GC analysis in the photoreduction of CO2 reaction of the sample of Co/g-C_3N_4-0.2 SAC after light irradiation 4 h.

1.19 TG experiment and characterizations for reused sample

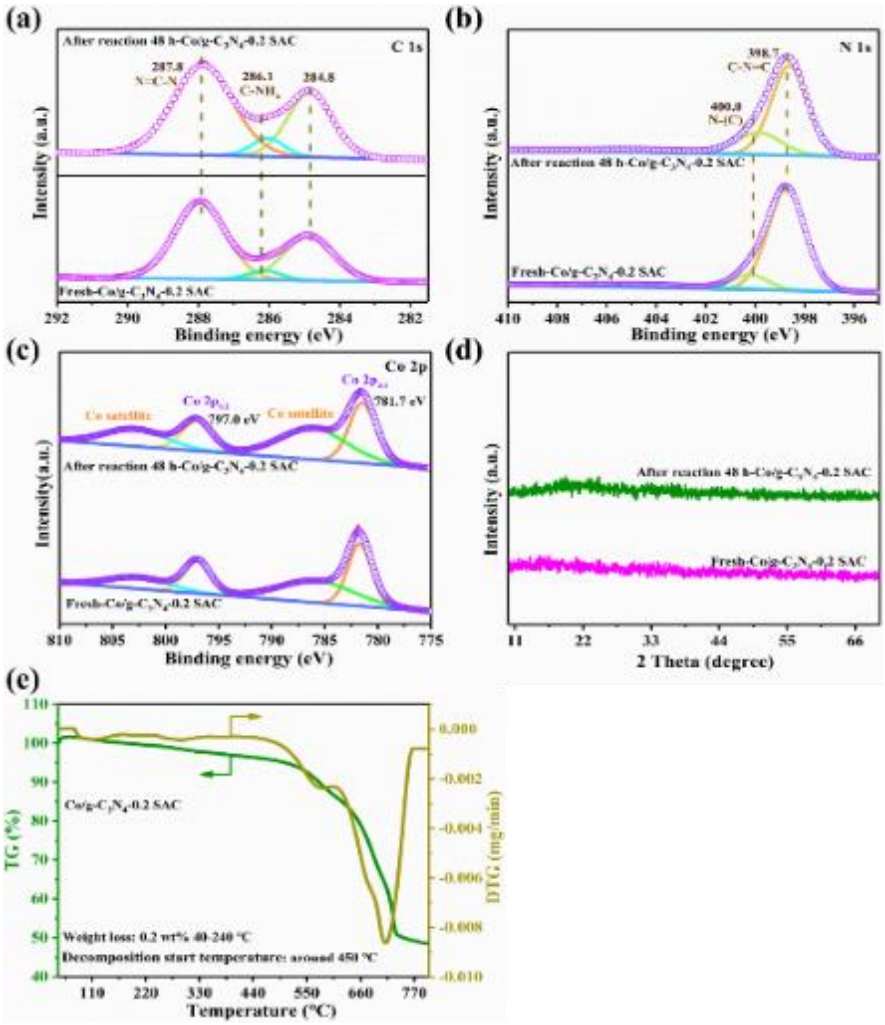

Figure S19. High-resolution C 1s (a), N 1s (b), and (c) Co 2p XPS spectra of Co/g-C_3N_4-0.2 SAC after reaction 48 h; (e) XRD patterns of photocatalysts; (e) TG curves of Co/g-C_3N_4-0.2 SAC.

1.20 Tauc plots

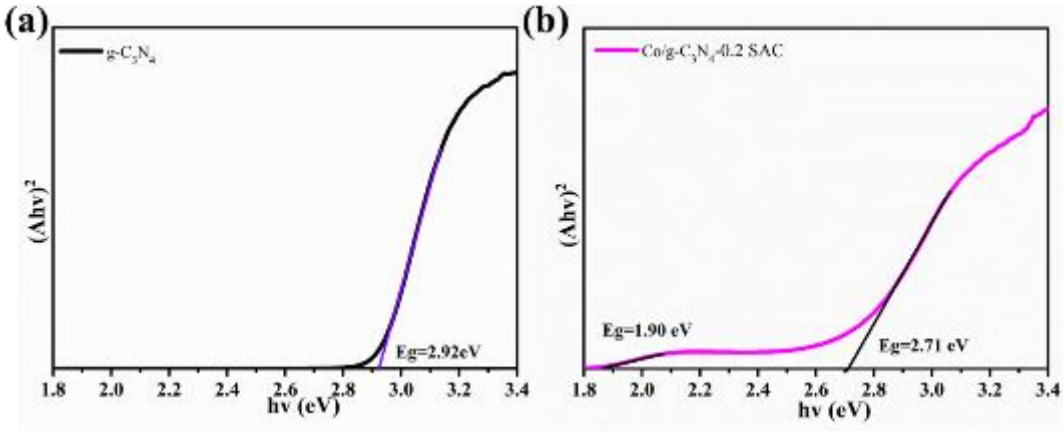

Figure S20. Tauc plots of the three samples. (a) g-C_3N_4, (b) Co/g-C_3N_4-0.2 SAC.

1.21 Elemental analysis

Table S1. The ICP-AES results for cobalt element and EA results for C, N, H, O, and S elements.

Samples	**Content of element (wt %)**						**Molar ratio (at %)**		
	Co	N	C	H	O	S	Total	C/N	Co
g-C_3N_4-NSs	-	52.0	25.0	2.8	24.2	0.6	104.6	0.56	-
g-C_3N_4	-	54.4	28.9	2.4	15.3	0.1	101.1	0.62	-
Co/g-C_3N_4-0.10	14.3	43.5	24.9	1.8	14.9	0.8	100.2	0.68	3.0
Co/g-C_3N_4-0.20	29.3	38.7	21.8	1.4	9.4	0.8	101.4	0.66	6.8
Co/g-C_3N_4-0.25	36.1	31.8	17.6	1.6	13.4	0.7	101.2	0.65	8.9

1.22 The Co K-edge EXAFS fitting parameters

Table S2. Structural parameters obtained from the Co K-edge EXAFS fits.

Samples	bonds	CN	R (Å)	$\sigma^2(10^{-3}$ Å$^2)$	△E (eV)	χ_v^2 / R factor	S_0^2
Co	Co-Co	12 [f]	2.49(±0.02)	6.6(±3.1)	6.7(±0.8)	273/0.0003	0.87
$Co(NO_3)_2$	Co-O	6 [f]	2.07(±0.01)	6.6(±1.1)	3.5(±1.1)	98/0.001	0.70 [f]
CoO	Co-O	6 [f]	2.08(±0.06)	9.3(±3.7)	6.9(±1.9)	371/0.004	0.87
	Co-Co	12[f]	2.96(±0.06)	9.3(±3.7)	6.9(±1.9)		
Co_3O_4	Co-O	6 [f]	1.96(±0.05)	3.0 [f]	-0.8(±1.9)	5/0.005	0.70 [f]
	$Co\text{-}Co_1$	6 [f]	2.91(±0.06)	4.7(±1.0)	-0.3(±3.4)		
	$Co\text{-}Co_2$	6 [f]	3.38(±0.04)	3.5(±1.1)	-8.6(±4.0)		
Co/g-C_3N_4-0.2	Co-N	2 [f]	2.07(±0.03)	6.2(±1.3)	9.3(±2.8)	240/0.009	1.00 [f]
SAC	Co-C	1 [f]	2.21(±0.04)	1.4(±2.5)	9.3(±2.8)		

f – Fixed to the given set value during the fit. The corresponding error bars are given in brackets.

1.23 Recent reported SACs with high metal loading (> 10 wt%).

Table S3. Recent advances for SACs with different metal loadings.

Materials	Loading [wt%, ICP]	Ref.	Materials	Loading [wt%, ICP]	Ref.
Co/g-C_3N_4 SAC	29.3 (XPS 24.6)	This work	SCoNC	15.3	[1]
Co–NC SAC	12.1	[2]	h-Pt_1-CuS_x	24.8 at%	[3]
HPC-800	11.3	[3]	NiSA-N-CNTs	20.3 (EDS)	[4]
SAS-Fe	30.0	[5]	SWNT/Pt	10.2 (XPS)	[6]
Cu–N–C	20.9	[7]	Co@Co-N-C-A NHs	19.4	[8]

1.24 BET results

Table S4. The surface area, pore structure parameters, and particles size.

Samples	S_{BET}(m^2/g)	pore volume (cm^3/g)	pore size (nm)
g-C_3N_4	5.0	0.016	12.9
g-C_3N_4-NSs	22.2	0.16	28.4
Co/g-C_3N_4-0.1 SAC	18.6	0.12	13.8
Co/g-C_3N_4-0.2 SAC	70.4	0.37	21.0
Co/g-C_3N_4-0.25	29.2	0.21	9.4
CoO_x/g-C_3N_4-0.2	27.7	0.13	19.2

1.25 Compared with the reported work

Table S5. Comparison of photocatalytic activity of Co/g-C_3N_4 SAC with other photocatalyst.

Photocatalyst	conditions	sacrificial agent	CO production rate (μmol g^{-1} h^{-1})	CH_4 rate (μmol g^{-1} h^{-1})	CH_3OH rate (μmol g^{-1} h^{-1})	Ref.
Co/g-C_3N_4-0.2	Catalyst: 5 mg; CO_2: 99.999 %; Water:1 mL; Light source: 300W Xe lamp	-	2.9	3.4	235.5	This work
$Zn_xCd_{1-x}S$/Au@g-C_3N_4	Catalyst: 50 mg; CO_2: 99.99 9%; Water: vapor; $NaHCO_3$: 0.084 g; H_2SO_4: aqueous solution (0.3 mL, 0.2 M) Light source: 300W Xe lamp with a 420 nm cut off filter.	-	-	-	1.31	[9]
RuSA–mC_3N_4	Catalyst: 50 mg CO_2: saturating the solution with CO_2, water and DMF mixture;Blue LED grow Light, wavelength range 400-500-34W (1.5A, H150, kessil)	-	-	-	250	[10]
α-Fe_2O_3/g-C_3N_4	Catalyst: 10 mg; CO_2: 99.99 9%; Water:40 mL; Light source: 300W Xe lamp with a 420 nm cut off filter	-	-	-	5.63	[11]
$Zn_{0.2}Cd_{0.8}S$/g-C_3N_4	Catalyst: 10 mg; CO_2: 99.99 9%; Water:20 mL; Light source: 300W Xe lamp with a 420 nm cut off filter	-	-	-	11.5	[12]
mCD/CN	Catalyst: 10 mg; CO_2: 99.99 9%; Water:10	-	-	-	13.9	[13]

	mL; Light source: 300W Xe lamp					
a-Mo/C_3N_4	Catalyst: 50 mg; CO_2: 99.99 9%; Water:20 mL; Light source: 300W Xe lamp with a 420 nm cut off filter	-	18	0.13	0	[14]
Co^{2+}@C_3N_4	Catalyst: 1 mg; CO_2: 99.999 %; Acetonitrile: 4 ml, bubble CO_2; Light source: halogen lamp with a 420 nm cut off filter	Triethanolamine	30	-	0	[15]
Co-porphyrin/PCN	CO_2: 99.999 %; Acetonitrile: 4 ml, CO_2: 80 kPa; Light source: 300W Xe lamp with $400 < \lambda < 800$ nm	Triethanolamine	17	0.7	0	[16]
MOF-525-Co	Catalyst: 2 mg; CO_2: 99.999%; Acetonitrile: 2 ml, bubble CO_2; Light source: 300W Xe lamp with a $400 < \lambda < 800$ nm cut off filter	Triethanolamine	200.6	36.7	0	[17]
Co–Bi_3O_4Br	Catalyst: 30 mg; CO2: 99.999 %; Water:50 mL; Light source: 300W Xe lamp	-	107.1	-	0	[18]

Supplementary References

[1] J.B. Wu, H. Zhou, Q. Li, M. Chen, J. Wan, N.A. Zhang, L.K. Xiong, S. Li, B.Y. Xia, G. Feng, M.L. Liu, L. Huang, Adv. Energy Mater. 9 (2019).

[2] L. Zhao, Y. Zhang, L.B. Huang, X.Z. Liu, Q.H. Zhang, C. He, Z.Y. Wu, L.J. Zhang, J. Wu, W. Yang, L. Gu, J.S. Hu, L.J. Wan, Nat. Commun. 10 (2019) 1278.

[3] R. Shen, W. Chen, Q. Peng, S. Lu, L. Zheng, X. Cao, Y. Wang, W. Zhu, J. Zhang, Z. Zhuang, C. Chen, D. Wang, Y. Li, Chem 5 (2019) 2099-2110.

[4] Y. Cheng, S. Zhao, B. Johannessen, J.P. Veder, M. Saunders, M.R. Rowles, M. Cheng, C. Liu, M.F. Chisholm, R. De Marco, H.M. Cheng, S.Z. Yang, S.P. Jiang, Adv. Mater. 30 (2018) e1706287.

[5] Y. Xiong, W.M. Sun, P.Y. Xin, W.X. Chen, X.S. Zheng, W.S. Yan, L.R. Zheng, J.C. Dong, J. Zhang, D.S. Wang, Y.D. Li, Adv. Mater. 32 (2020) e2000896.

[6] M. Tavakkoli, N. Holmberg, R. Kronberg, H. Jiang, J. Sainio, E.I. Kauppinen, T. Kallio, K. Laasonen, ACS Catal. 7 (2017) 3121-3130.

[7] F. Li, G.-F. Han, H.-J. Noh, S.-J. Kim, Y. Lu, H.Y. Jeong, Z. Fu, J.-B. Baek, Energy Environ. Sci. 11 (2018) 2263-2269.

[8] S.L. Zhao, J. Yang, M. Han, X.M. Wang, Y. Lin, R. Yang, D.D. Xu, N.E. Shi, Q. Wang, M.J. Yang, Z.H. Dai, J.C. Bao, Appl. Catal. B: Enviorn. 260 (2020) 118207.

[9] P. Madhusudan, R. Shi, S. Xiang, M. Jin, B.N. Chandrashekar, J. Wang, W. Wang, O. Peng, A. Amini, C. Cheng, Appl. Catal. B: Enviorn. 282 (2021) 119600.

[10] P. Sharma, S. Kumar, O. Tomanec, M. Petr, J. Zhu Chen, J.T. Miller, R.S. Varma, M.B. Gawande, R. Zboril, Small 17 (2021) e2006478.

[11] H. Guo, M. Chen, Q. Zhong, Y. Wang, W. Ma, J. Ding, J. CO_2 Util. 33 (2019) 233-241.

[12] H. Guo, J. Ding, S. Wan, Y. Wang, Q. Zhong, Appl. Surf. Sci. 528 (2020) 146943.

[13] Y. Wang, X. Liu, X. Han, R. Godin, J. Chen, W. Zhou, C. Jiang, J.F. Thompson, K.B. Mustafa, S.A. Shevlin, J.R. Durrant, Z. Guo, J. Tang, Nat. Commun. 11 (2020) 2531.

[14] R.Y. Zhang, P.H. Li, F. Wang, L.Q. Ye, A. Gaur, Z.A. Huang, Z.Y. Zhao, Y. Bai, Y. Zhou, Appl. Catal. B: Enviorn. 250 (2019) 273-279.

[15] P. Huang, J. Huang, S.A. Pantovich, A.D. Carl, T.G. Fenton, C.A. Caputo, R.L. Grimm, A.I. Frenkel, G. Li, J. Am. Chem. Soc. 140 (2018) 16042-16047.

[16] G.X. Zhao, H. Pang, G.G. Liu, P. Li, H.M. Liu, H.B. Zhang, L. Shi, J.H. Ye, Appl. Catal. B: Enviorn. 200 (2017) 141-149.

[17]H.B. Zhang, J. Wei, J.C. Dong, G.G. Liu, L. Shi, P.F. An, G.X. Zhao, J.T. Kong, X.J. Wang, X.G. Meng, J. Zhang, J.H. Ye, Angew. Chem. Int. Ed. 55 (2016) 14308-14312.

[18] J. Di, C. Chen, S.Z. Yang, S. Chen, M. Duan, J. Xiong, C. Zhu, R. Long, W. Hao, Z. Chi, H. Chen, Y.X. Weng, J. Xia, L. Song, S. Li, H. Li, Z. Liu, Nat. Commun. 10 (2019) 2840.